Non-associated Reuleaux plasticity: analytical stress integration and consistent tangent for finite deformation mechanics

William M. Coombs[1] and Roger S. Crouch[1*]

[1] Durham University, School of Engineering and Computing Sciences, South Road, Durham, DH1 3LE, United Kingdom.

Abstract

Analytical backward Euler stress integration is presented for a volumetrically non-associated pressure-sensitive yield criterion based on a modified Reuleaux triangle. This advances previous work on associated Reuleaux plasticity using energy-mapped stress space. The analytical solution is 2-4 times faster than a standard numerical backward Euler algorithm. The merit in transforming to (and operating in) this space is that the stress return is truly the closest point on the surface to the elastic trial state. The paper includes a tension cut-off (formed by a second cone) and describes the steps necessary to allow the model's incorporation within a finite deformation framework. Finite-element results show a 59% runtime saving for a modified Reuleaux model over a Willam-Warnke cone giving comparable accuracy in a thick-walled cylinder expansion problem. The consistent tangent provides asymptotically quadratic convergence in the Newton-Raphson scheme under both (i) small strain, infinitesimal deformation and (ii) large strain, finite deformation finite-element simulations. It is shown that the introduction of non-associated flow changes the plastic deformation field and reduces the heave predicted in a plane strain rigid strip-footing problem. The proposed model offers a significant improvement over the Drucker-Prager and Mohr-Coulomb formulations by better reproducing the material dependence on the Lode angle and intermediate principal stress, at little extra computational effort.

Keywords: Closest point projection, computational plasticity, analytical stress return, consistent tangent, finite deformation mechanics, non-associated plastic flow

1 Introduction

This paper offers a compact analytical solution to the backward Euler stress integration for non-associated Reuleaux plasticity. The constitutive formulation is embedded within an updated Lagrangian, Kirchhoff stress-logarithmic strain, finite-element framework. The paper extends earlier work on (infinitesimal deformation) associated isotropic Reuleaux plasticity [7] by providing, for the first time, closed-form expressions for the Closest Point Projection (CPP) using Energy-Mapped Stress Space (EMSS) [8] for a volumetrically non-associated model incorporating a tension cut-off.

Section 2 gives the geometric-algebraic steps required to extend the energy mapped approach to include Non-Associated plastic Flow (NAF). All equations are derived (in Section 3) which lead to the backward Euler stresses and consistent tangent for the NAF Reuleaux model. The use of a second cone, to provide a tension cut-off, is explained in Section 4. Details of the updated Lagrangian finite deformation finite-element framework are given in Section 5. Error and runtime analyses for material point simulations are provided in Section 6, together with finite-element results for (i) the expansion of a thick-walled cylinder, (ii) the expansion of a cylindrical cavity and (iii) the load-deformation behaviour of a rigid strip footing, where associated and non-associated plastic strain contour plots and displacement vectors are compared for infinitesimal and finite deformation simulations. Final conclusions are drawn in Section 7.

In all that follows $\{\cdot\}$ and $[\cdot]$ denote vectors and matrices respectively, $[\dot{\cdot}]$ and $[\bar{\cdot}]$ identify terms associated with principal and shear components of generalised stiffness matrices and $\{\cdot\}^T$ denotes a vector transpose. We adopt a tension positive convention and order the principal stresses such that σ_1 is the most compressive, while σ_3 is the most tensile.

2 Energy-mapped stress space

Simo and Hughes [23] reported that the Backward Euler (BE) integration method corresponds to the "closest projection of the [trial elastic stress] onto the yield surface in the energy norm". In the paper by Crouch *et*

*corresponding author: Roger Crouch, Durham University, School of Engineering and Computing Sciences, South Road, Durham, DH1 3LE, United Kingdom. r.s.crouch@durham.ac.uk

al. [8], the concept of working in an EMSS was clarified. This space facilitates visualisation of the CPP stress return and reveals where analytical stress returns based purely on geometric methods are possible for certain yield surfaces. These concepts were used by Coombs *et al.* [7] to provide the analytical stress return for a new associated flow perfect plasticity pressure-dependent deviatoric yielding criterion based on a modified Reuleaux triangle. Previous work using EMSS was restricted to associated flow perfect plasticity with linear elasticity. For isotropic linear elastic media, the transformation between true stress space and EMSS is only dependent on the value of Poisson's ratio.

In the case of non-linear elasticity, the energy-mapped surface takes on additional curvature. For example, if a linear variation in bulk modulus with pressure and a constant shear modulus were adopted, then a Drucker-Prager cone would transform into a convex quadratic cone for which an analytical BE solution would be possible. For more complex forms (that is, nonlinear meridians and non-circular deviatoric cross-section) the solution would require a polynomial of 5^{th} order (or higher) to be solved numerically.

Although this paper examines perfectly plastic models, the EMSS still provides a valuable framework with which to view hardening/softening plasticity since the return point will remain closest to the trial point (for the case of associated flow) with respect to the evolving yield surface. The full range of hardening/softening models which retain analytic BE solutions has not yet been identified.

Within energy-mapped stress space, the NAF CPP solution corresponds to that stress state on the yield surface where the normal to the plastic potential passes through the trial stress state (see Figure 1). Once the closest point in energy-mapped stress space has been found, that solution can be transformed back to conventional stress space. Note that for an isotropic model we need only operate with principal stresses (conventional and energy-mapped) during the integration process.

For details on the transformation of stress states into EMSS see Crouch *et al.* [8] (or Coombs *et al.* [7] for the particular case of the modified Reuleaux cone). The equations have been omitted from this paper for sake of brevity. In all that follows ${}^{\varsigma}(\cdot)$ denotes quantities associated with the EMSS.

3 Non-associated modified Reuleaux plasticity

This section describes the NAF modified Reuleaux cone; presenting the analytical stress returns and the consistent tangents for the three return regions within EMSS.

3.1 Defining equations

Haigh-Westergaard cylindrical coordinates ξ, ρ and θ are adopted, where $\xi = \text{tr}[\sigma]/\sqrt{3}$, $\rho = \sqrt{2J_2}$, $J_2 = (\text{tr}[s]^2)/2$, $J_3 = (\text{tr}[s]^3)/3$, $[s] = [\sigma] - \xi[1]/\sqrt{3}$. tr$[\cdot]$ is the trace and $[1]$ denotes the $3{\times}3$ identity matrix. The Lode angle is given by

$$\theta = \frac{1}{3}\arcsin\left(\frac{-3\sqrt{3}}{2}\frac{J_3}{J_2^{3/2}}\right) \qquad \in \Big[-\pi/6, \pi/6\Big]. \tag{1}$$

From geometric considerations (see Figure 2 (i) and [7]) the modified Reuleaux (MR) Lode angle dependency may be obtained as

$$\overline{\rho}(\theta) = \sqrt{\overline{a}^2 + \overline{r}^2 - 2\overline{a}\,\overline{r}\cos(\phi)}, \tag{2}$$

where

$$\overline{r} = \frac{\overline{\rho}_e^2 - \overline{\rho}_e + 1}{2\overline{\rho}_e - 1}, \qquad \overline{a} = \overline{r} - \overline{\rho}_e, \qquad \overline{\rho}_e = \frac{\rho_e}{\rho_c} \qquad \text{and} \qquad \overline{\rho} = \frac{\rho}{\rho_c}. \tag{3}$$

ρ_c denotes the deviatoric radius on the compression meridian ($\theta = \pi/6$). $\overline{\rho}_e \in [0.5, 1]$ gives the relative size of the radius under triaxial extension ($\sigma_1 = \sigma_2 < \sigma_3$) with respect to that under triaxial compression ($\sigma_1 < \sigma_2 = \sigma_3$) at a given ξ. The arc angle, ϕ, is defined as

$$\phi = \frac{\pi}{6} + \theta - \arcsin\left(\frac{\overline{a}\sin(5\pi/6 - \theta)}{\overline{r}}\right). \tag{4}$$

If the arc centres are located on the yield surface compression meridians (that is, if $\overline{r} = 1 + \overline{\rho}_e$ so that $\overline{a} = 1$) then the shape of the deviatoric section is a Reuleaux triangle. Allowing the location of the arc centres to vary along projections of the compression meridians gives rise to the *modified Reuleaux triangle*. As $\overline{\rho}_e \to 0.5$ both $\overline{r}$ and $\overline{a}$ tend to ∞ and the deviatoric section becomes an equilateral triangle. If $\overline{\rho}_e = 1$ then $\overline{\rho} = 1$ and we recover a circular deviatoric section centred on the hydrostatic axis (as found in the Drucker-Prager, D-P, model).

The MR cone can be defined as

$$f = \rho - \alpha\overline{\rho}\Big(\xi - \xi_c\Big) = 0, \tag{5}$$

where ξ_c is the intersection of the yield surface with the hydrostatic axis and α is the opening angle of the cone, $\alpha = -\tan(\psi_{MC})$. ψ_{MC} is the Mohr-Coulomb (M-C) internal friction angle of the material under triaxial compression. Thus (5) defines a cone with a MR deviatoric section and linear meridians, pinned on the hydrostatic axis at ξ_c with that space diagonal ($\sigma_1 = \sigma_2 = \sigma_3$) providing the cone's axis, see Figure 2 (ii). The MR cone can be seen as a hybrid surface, lying between the D-P and M-C envelopes, allowing some control over the shape of the deviatoric section, independent of the cone opening angle. This formulation provides a dependency on both the Lode angle (θ) and the intermediate principal stress (σ_2). The D-P surface includes a dependance on σ_2 but not on the Lode angle, whereas, the M-C surface includes a dependency on the Lode angle but not σ_2. Real materials exhibit dependencies on both [3, 22]. In rocks, the influence of θ is most clearly seen in the biaxial plane where yield surfaces which neglect this measure provide poor fits to experimental data. Intermediate principal stress values close to the most compressive principal stress confine microfractures to develop mainly in the plane formed by the direction of those two stresses [11]. The formulation of compaction bands [13] and fault slip patterns in complex fracture fields [20] have also recently been shown to be controlled by σ_2. Thus its inclusion in a geomechanics model is now considered essential. Further advantages of the MR model are demonstrated in [7].

It is widely accepted that associated frictional plasticity models overestimate the dilation seen in particulate media. To overcome this shortfall, the following plastic potential is adopted

$$g = \rho - \beta\overline{\rho}\Big(\xi - \xi_g\Big) = 0, \tag{6}$$

where ξ_g is the intersection of the plastic potential with the hydrostatic axis and $\beta = -\tan(\psi_g)$ is the opening angle of the plastic potential surface. ψ_g gives the dilation angle under triaxial compression, $\psi_g \in [0, \psi_{M-C}]$. Combining (5) and (6) gives rise to a perfect plasticity model with non-associated volumetric plastic flow but associated deviatoric plasticity. The plastic potential is defined such that it intersects any stress state on the yield surface f. To achieve this

$$\xi_g = \xi - \frac{\alpha}{\beta}(\xi - \xi_c), \tag{7}$$

where ξ is the hydrostatic stress of the point on the yield surface.

Consider the trial elastic stress $\{\sigma_t\}$ (given by a trial elastic strain $\{\varepsilon_t^e\}$) lying outside the yield surface ($f > 0$). For this state, there are three distinct stress return regions associated with the MR cone, as shown in Figure 2 (ii), namely:

A. Return to the stress origin (point): Apex return,

B. Return to the compression meridian (line): Edge return,

C. Return to the surface: Non-planar surface return.

The CPP solution and consistent tangent are considered for each of the above regions in Sections 3.2-3.4. Figure 4 describes the numerical implementation. The energy-mapped opening angles of the yield surface and plastic potential (see Section 2 above), ${}^{\varsigma}\alpha$ and ${}^{\varsigma}\beta$, are given by

$${}^{\varsigma}\alpha = \frac{\alpha\sqrt{1+v}}{\sqrt{1-2v}} \qquad \text{and} \qquad {}^{\varsigma}\beta = \frac{\beta\sqrt{1+v}}{\sqrt{1-2v}} \tag{8}$$

respectively. Throughout the following, and without loss of generality, the yield surface is assumed to be pinned at the stress origin, $\xi_c = 0$. For cases where $\xi_c \neq 0$ the trial stress state can be hydrostatically translated by ξ_c in order to accommodate a tensile apex.

3.2 Apex return

If ${}^{\varsigma}f_a < 0$ then the trial stress point $\{\varsigma_t\}$ will be returned onto the apex of the MR cone, with

$$\{\varsigma_{cp}\} = (\{\sigma_{cp}\} = \xi_c/\sqrt{3})\{1\}, \tag{9}$$

where $(\cdot)_{cp}$ denotes quantities associated with the closest point and $\{1\} = \{1 \quad 1 \quad 1\}^T$. The apex boundary function is given by

$${}^{\varsigma}f_a = {}^{\varsigma}\rho + \frac{1}{{}^{\varsigma}\beta\overline{\rho}}\Big({}^{\varsigma}\xi - {}^{\varsigma}\xi_c\Big) = 0. \tag{10}$$

3.2.1 Apex consistent tangent

As Clausen *et al.* have shown [5], the elasto-plastic consistent tangent for a hydrostatic apex return is simply

$$\left[D^{alg}\right] = [0]. \tag{11}$$

3.3 Edge return

For trial stresses outside the yield surface returning onto the compression meridian

$$\theta_{cp} = \pi/6 \qquad \text{and} \qquad {}^{\varsigma}\rho_{cp} = {}^{\varsigma}\alpha\,{}^{\varsigma}\xi_{cp}. \tag{12}$$

One obtains the solution for this case by recognising that the return vector from the trial point will be orthogonal to the direction of the plastic potential compression meridian line in EMSS. Therefore we may write

$$\{{}^{\varsigma}n\}^T\big\{\{\varsigma_{cp}\} - \{\varsigma_t\}\big\} = 0, \tag{13}$$

where $\{{}^{\varsigma}n\}$ is this normal, given by

$$\{{}^{\varsigma}n\} = \Big\{1 - \sqrt{2}\,{}^{\varsigma}\beta \qquad 1 + {}^{\varsigma}\beta/\sqrt{2} \qquad 1 + {}^{\varsigma}\beta/\sqrt{2}\Big\}^T. \tag{14}$$

An edge point of the energy-mapped yield surface is given by

$$\{\varsigma\} = \frac{{}^{\varsigma}\xi}{\sqrt{3}}\Big\{1 - \sqrt{2}\,{}^{\varsigma}\alpha \qquad 1 + {}^{\varsigma}\alpha/\sqrt{2} \qquad 1 + {}^{\varsigma}\alpha/\sqrt{2}\Big\}^T. \tag{15}$$

Substituting (14) and (15), for $\{\varsigma_{cp}\}$, into (13), we obtain an equation which can be solved for ${}^{\varsigma}\xi_{cp}$

$${}^{\varsigma}\xi_{cp} = \frac{(\varsigma_{t_2} + \varsigma_{t_3})\left(1 + {}^{\varsigma}\beta/\sqrt{2}\right) + \varsigma_{t_1}\left(1 - \sqrt{2}\,{}^{\varsigma}\beta\right)}{\sqrt{3}(1 + {}^{\varsigma}\alpha\,{}^{\varsigma}\beta)}. \tag{16}$$

Subsequently ${}^{\varsigma}\xi_{cp}$ and ${}^{\varsigma}\rho_{cp}$ can be transformed back into conventional principal stress space to calculate the final return stress $\{\sigma_{cp}\}$ using the Haigh-Westergaard expression

$$\{\sigma\} = \frac{\xi}{\sqrt{3}}\{1\} + \sqrt{\frac{2}{3}}\rho\Big\{\sin(\theta - 2\pi/3) \qquad \sin(\theta) \qquad \sin(\theta + 2\pi/3)\Big\}^T. \tag{17}$$

These stresses are then transformed back to generalised stress space through use of the eigenvectors associated with the generalised trial stress state.

3.3.1 Edge consistent tangent

The consistent tangent for an edge return is obtained following the approach given by Clausen *et al.* [6]. By considering the vector orientation of the yield surface edge

$$\{n_f\} = \Big\{1 - \sqrt{2}\alpha \qquad 1 + \alpha/\sqrt{2} \qquad 1 + \alpha/\sqrt{2}\Big\}^T, \tag{18}$$

and that of the plastic potential

$$\{n_g\} = \Big\{1 - \sqrt{2}\beta \qquad 1 + \beta/\sqrt{2} \qquad 1 + \beta/\sqrt{2}\Big\}^T, \tag{19}$$

we obtain the 3×3 (that is, in principal form) infinitesimal elasto-plastic tangent matrix as

$$\left[\hat{D}^{ep}\right] = \frac{\{n_f\}\{n_g\}^T}{\{n_f\}^T\left[\hat{C}^{\mathrm{e}}\right]\{n_g\}}, \tag{20}$$

where $\left[\hat{C}^{\mathrm{e}}\right]$ is the 3×3 (principal) elastic compliance matrix. The 6×6 elasto-plastic tangent matrix is then given by

$$\left[D^{ep}\right] = \begin{bmatrix} \left[\hat{D}^{ep}\right] & [0] \\ [0] & (E/2(1+v))\,[1] \end{bmatrix}. \tag{21}$$

The consistent tangent follows as

$$\left[D^{alg}\right] = \left[Q\right]\left[D^{ep}\right], \tag{22}$$

where $\left[Q\right]$ is given by

$$[Q] = \begin{bmatrix} [1] & [0] \\ [0] & [\overline{Q}] \end{bmatrix}. \tag{23}$$

Using the fact that $\sigma_2 = \sigma_3$ for a return onto the edge, $[\overline{Q}]$ was shown in [7] to be equal to

$$[\overline{Q}] = \begin{bmatrix} \frac{\sigma_1 - \sigma_2}{\sigma_{t_1} - \sigma_{t_2}} & 0 & 0 \\ 0 & 0 & 0 \\ 0 & 0 & \frac{\sigma_1 - \sigma_3}{\sigma_{t_1} - \sigma_{t_3}} \end{bmatrix}, \tag{24}$$

where σ_{t_i} are the principal trial stresses. From (22) and (24) the consistent tangent, for the edge return, can be written as

$$\left[D^{alg}\right] = \begin{bmatrix} \left[\hat{D}^{ep}\right] & [0] \\ [0] & (E/2(1+v))\left[\overline{Q}\right] \end{bmatrix}. \tag{25}$$

Once the consistent tangent has been formed in principal stress space (25) it must be transformed back to generalised stress space, see Clausen *et al.* for further details [5].

3.4 Non-planar surface return

Assuming that a trial elastic stress $\{\varsigma_t\}$ outside the yield will return onto the non-singular portion of the yield surface, we can define the square of the distance between that trial point and a point on the surface at the same ϕ_t in any deviatoric plane at a given ${}^{\varsigma}\xi_t$ (see Figure 3) as

$$l^2 \;=\; (r_t - r)^2 + ({}^{\varsigma}\xi - {}^{\varsigma}\xi_t)^2. \tag{26}$$

Substituting $r = \overline{r}\,{}^{\varsigma}\beta({}^{\varsigma}\xi - {}^{\varsigma}\xi_g)$ and

$$r_t^2 = a^2 + {}^{\varsigma}\rho_t^2 - 2a\,{}^{\varsigma}\rho_t C \qquad \Big(\text{where} \quad C = \cos(5\pi/6 - \theta_t) \quad \text{and} \quad a = \overline{a}\,{}^{\varsigma}\beta({}^{\varsigma}\xi - {}^{\varsigma}\xi_g)\Big) \tag{27}$$

into (26), taking the partial derivative of l^2 with respect to ${}^{\varsigma}\xi$ and setting that derivative equal to zero, we obtain

$$\begin{aligned} \frac{\partial l^2}{\partial\,{}^{\varsigma}\xi} \;=\; & \overline{a}^2\,{}^{\varsigma}\beta^2\,{}^{\varsigma}\xi r_t - \overline{a}^2\,{}^{\varsigma}\beta^2\,{}^{\varsigma}\xi_g r_t - \overline{a}\,{}^{\varsigma}\beta\,{}^{\varsigma}\rho_t C r_t - r_t^2\overline{r}\,{}^{\varsigma}\beta - \ldots \\ & -\overline{r}\,{}^{\varsigma}\beta({}^{\varsigma}\xi - {}^{\varsigma}\xi_g)(\overline{a}^2\,{}^{\varsigma}\beta^2\,{}^{\varsigma}\xi - \overline{a}^2\,{}^{\varsigma}\beta^2\,{}^{\varsigma}\xi_g - \overline{a}\,{}^{\varsigma}\beta\,{}^{\varsigma}\rho_t C) + ({}^{\varsigma}\xi\overline{r}^2\,{}^{\varsigma}\beta^2 - {}^{\varsigma}\xi_g\overline{r}^2\,{}^{\varsigma}\beta^2 + {}^{\varsigma}\xi - {}^{\varsigma}\xi_t)r_t = 0. \end{aligned} \tag{28}$$

Note that throughout the partial differentiation we ignore the dependance of ${}^{\varsigma}\xi_g$ on ${}^{\varsigma}\xi$. Through manipulation and substituting ${}^{\varsigma}\xi_g$ from (7) (with $\xi_c = 0$) into (28), we obtain the following quartic in ${}^{\varsigma}\xi_{cp}$

$${}^{\varsigma}\xi_{cp}^4 A_1 + {}^{\varsigma}\xi_{cp}^3 A_2 + {}^{\varsigma}\xi_{cp}^2 A_3 + {}^{\varsigma}\xi_{cp} A_4 + A_5 = 0, \tag{29}$$

where

$$\begin{aligned} A_1 &= \overline{a}^2\,{}^{\varsigma}\alpha^2 B_1^2 - 4\overline{a}^4\overline{r}^2\,{}^{\varsigma}\alpha^4\,{}^{\varsigma}\beta^2, \\ A_2 &= 12\overline{a}^3\overline{r}^2\,{}^{\varsigma}\alpha^3\,{}^{\varsigma}\beta^2\rho_t C - 2\overline{a}^2\,{}^{\varsigma}\alpha^2 B_1 B_2 - 2\overline{a}\,{}^{\varsigma}\alpha\,{}^{\varsigma}\rho_t C B_1^2, \\ A_3 &= \overline{a}^2\,{}^{\varsigma}\alpha^2 B_2^2 + {}^{\varsigma}\rho_t^2 B_1^2 + 4\overline{a}\,{}^{\varsigma}\alpha\,{}^{\varsigma}\rho_t C B_1 B_2 - 9\overline{a}^2\overline{r}^2\,{}^{\varsigma}\alpha^2\,{}^{\varsigma}\beta^2\,{}^{\varsigma}\rho_t^2 C^2 - 4\overline{a}^2\overline{r}^2\,{}^{\varsigma}\alpha^2\,{}^{\varsigma}\beta^2\,{}^{\varsigma}\rho_t^2, \\ A_4 &= 6\overline{a}\overline{r}^2\,{}^{\varsigma}\alpha\,{}^{\varsigma}\beta^2\,{}^{\varsigma}\rho_t^3 C - 2\,{}^{\varsigma}\rho_t^2 B_1 B_2 - 2\overline{a}\,{}^{\varsigma}\alpha\,{}^{\varsigma}\rho_t C B_2^2, \\ A_5 &= {}^{\varsigma}\rho_t^2 B_2^2 - {}^{\varsigma}\rho_t^4\overline{r}^2\,{}^{\varsigma}\beta^2, \end{aligned}$$

$$\begin{aligned} B_1 &= \overline{a}^2\,{}^{\varsigma}\alpha\,{}^{\varsigma}\beta + \overline{r}^2\,{}^{\varsigma}\alpha\,{}^{\varsigma}\beta + 1, \\ B_2 &= \overline{a}\,{}^{\varsigma}\beta\,{}^{\varsigma}\rho_t C + \xi_t. \end{aligned}$$

This quartic can be solved for ${}^{\varsigma}\xi_{cp}$ (see Simo and Hughes page 138 [24], amongst others, for more details). Once ${}^{\varsigma}\xi_{cp}$ is known, then the other quantities identifying the position of the closest point on the MR surface can be calculated. ϕ_{cp} is given by the sine rule

$$\phi_{cp} = \arcsin\left(\frac{{}^{\varsigma}\rho_t \sin(5\pi/6 - \theta_t)}{r_t}\right), \tag{30}$$

where r_t is calculated at the solution ${}^{\varsigma}\xi_{cp}$ using (27). ${}^{\varsigma}\rho_{cp} = {}^{\varsigma}\alpha\overline{\rho}(\theta){}^{\varsigma}\xi_{cp}$ with $\overline{\rho}(\theta)$ given by (2) and θ_{cp} determined from the cosine rule

$$\theta_{cp} = \frac{5\pi}{6} - \arccos\left(\frac{a_{cp}^2 + {}^{\varsigma}\rho_{cp}^2 - r_{cp}^2}{2a_{cp}\,{}^{\varsigma}\rho_{cp}}\right), \tag{31}$$

r_{cp} and a_{cp} are values associated with ${}^{\varsigma}\xi_{cp}$. The stress return for the non-associated MR cone is equivalent to the closest point to the plastic potential in energy-mapped space. The yield and plastic potential surfaces coincide at the return stress state.

3.4.1 Non-planar consistent tangent

The consistent tangent for the non-associated surface return is calculated by minimising

$$\left\{ \begin{array}{c} \{\varepsilon^{\mathrm{e}}\} - \{\varepsilon_t^{\mathrm{e}}\} + \Delta\gamma\{g_{,\sigma}\} \\ f \end{array} \right\} = \left\{ \begin{array}{c} \{0\} \\ 0 \end{array} \right\}, \tag{32}$$

with respect to $\{\varepsilon_t^{\mathrm{e}}\}$, thereby obtaining

$$\left[\begin{array}{cc} \left[\hat{C}^{\mathrm{e}}\right] + \Delta\gamma[g_{,\sigma\sigma}] & \{g_{,\sigma}\} \\ \{f_{,\sigma}\}^T & 0 \end{array} \right] \left\{ \begin{array}{c} \{d\sigma\} \\ d\Delta\gamma \end{array} \right\} = \left\{ \begin{array}{c} \{d\varepsilon_t^{\mathrm{e}}\} \\ 0 \end{array} \right\}. \tag{33}$$

Rearranging, we have

$$\left\{ \begin{array}{c} \{d\sigma\} \\ d\Delta\gamma \end{array} \right\} = \left[\begin{array}{cc} [D^{alg}] & \{D_{12}\} \\ \{D_{21}\} & D_{22} \end{array} \right] \left\{ \begin{array}{c} \{d\varepsilon_t^{\mathrm{e}}\} \\ 0 \end{array} \right\}, \tag{34}$$

where $(\cdot)_{,\sigma}$ and $(\cdot)_{,\sigma\sigma}$ in (32) and (33) denote the first and second partial derivatives of $(\cdot)$ with respect to $\{\sigma\}$. We assume that the yield surface apex lies at the stress origin ($\xi_c = 0$) when taking derivatives with respect to $\{\sigma\}$. For cases where $\xi_c \neq 0$ the trial stress state is hydrostatically shifted such that $\xi_c = 0$ and then the return stresses are hydrostatically translated back by the original ξ_c amount. The first derivative of the yield function f, from (5), is given by

$$\{f_{,\sigma}\} = \{\rho_{,\sigma}\} - \alpha\xi\{\overline{\rho}_{,\sigma}\} - \alpha\overline{\rho}\{\xi_{,\sigma}\}. \tag{35}$$

Operating only with the derivatives with respect to the principal stresses; $\{\rho_{,\sigma}\} = \{s\}/\rho$ and $\{\xi_{,\sigma}\} = \{1\}/\sqrt{3}$. The derivative of $\overline{\rho}$ with respect to $\{\sigma\}$ is given by

$$\{\overline{\rho}_{,\sigma}\} = \overline{\rho}_{,\overline{\rho}\overline{\rho}}\ \overline{\rho}^2_{,\phi}\ \phi_{,\theta}\,\{\theta_{,\sigma}\}, \tag{36}$$

where

$$\overline{\rho}_{,\overline{\rho}\overline{\rho}} = \frac{1}{2\overline{\rho}}, \qquad \overline{\rho}^2_{,\phi} = 2\overline{a}\,\overline{r}\sin\phi \qquad \text{and} \qquad \phi_{,\theta} = 1 + \frac{\overline{a}\cos(5\pi/6-\theta)}{\overline{r}\sqrt{1-(\overline{a}\sin(5\pi/6-\theta)/\overline{r})^2}}. \tag{37}$$

The derivative of the Lode angle with respect to stress $\{\theta_{,\sigma}\}$ is given in [7]. The derivative of the yield function with respect to stress (35) can be split into volumetric and deviatoric components

$$\{f_{,\sigma}\} = \underbrace{\{\rho_{,\sigma}\} - \alpha\xi\{\overline{\rho}_{,\sigma}\}}_{\{f^{dev}_{,\sigma}\}} - \underbrace{\alpha\overline{\rho}\{\xi_{,\sigma}\}}_{\{f^{vol}_{,\sigma}\}}, \tag{38}$$

allowing the derivative of the plastic potential (6) with respect to $\{\sigma\}$ to be defined as

$$\{g_{,\sigma}\} = \{g^{dev}_{,\sigma}\} - \{g^{vol}_{,\sigma}\}, \tag{39}$$

where

$$\{g^{dev}_{,\sigma}\} = \{f^{dev}_{,\sigma}\} \qquad \text{and} \qquad \{g^{vol}_{,\sigma}\} = \beta\overline{\rho}\{\xi_{,\sigma}\}. \tag{40}$$

The second derivative of (6) with respect to stress is given by

$$[g_{,\sigma\sigma}] = [\rho_{,\sigma\sigma}] - (\alpha+\beta)\{\xi_{,\sigma}\}\{\overline{\rho}_{,\sigma}\}^T - \alpha\xi[\overline{\rho}_{,\sigma\sigma}], \tag{41}$$

where

$$\left[\rho_{,\sigma\sigma}\right] = \frac{\rho\left[J_{2,\sigma\sigma}\right] - \{\rho_{,\sigma}\}\{s\}^T}{\rho^2}, \tag{42}$$

and $[J_{2,\sigma\sigma}]$ can be found in [7]. Second derivatives of $\overline{\rho}$ and ϕ follow as shown

$$\left[\overline{\rho}_{,\sigma\sigma}\right] = \{\overline{\rho}_{,\sigma\overline{\rho}}\}\{\overline{\rho}_{,\sigma}\}^T + \{\overline{\rho}_{,\sigma\phi}\}\{\phi_{,\sigma}\}^T + \overline{\rho}_{,\sigma\phi,\sigma}\left[\phi_{,\sigma\sigma}\right], \tag{43}$$

$$\{\overline{\rho}_{,\sigma\overline{\rho}}\} = -\frac{\overline{ar}\sin\phi}{\overline{\rho}^2}\{\phi_{,\sigma}\}, \qquad \{\overline{\rho}_{,\sigma\phi}\} = \frac{\overline{ar}\cos\phi}{\overline{\rho}}\{\phi_{,\sigma}\}, \qquad \overline{\rho}_{,\sigma\phi,\sigma} = \frac{\overline{ar}\sin\phi}{\overline{\rho}} \qquad \text{and} \tag{44}$$

$$\left[\phi_{,\sigma\sigma}\right] = \{\phi_{,\sigma\theta}\}\{\theta_{,\sigma}\}^T + \phi_{,\theta}\left[\theta_{,\sigma\sigma}\right], \tag{45}$$

where

$$\{\phi_{,\sigma\theta}\} = \frac{\overline{a}}{\overline{r}}\left(\frac{S\overline{r}^2\left(1-(S\overline{a}/\overline{r})^2\right)^2 - \overline{a}^2SC^2}{\overline{r}^2(1-(S\overline{a}/\overline{r})^2)\sqrt{1-(S\overline{a}/\overline{r})^2}}\right)\{\theta_{,\sigma}\}. \tag{46}$$

Here $C = \cos(5\pi/6-\theta)$ and $S = \sin(5\pi/6-\theta)$. The second derivative of θ with respect to $\{\sigma\}$ is given by Coombs *et al.* [7]. We now have the all derivatives required for (34). These have been determined in principal stress form. The full 6×6 consistent tangent is given by

$$\left[D^{alg}\right] = \begin{bmatrix} \left[\hat{D}^{alg}\right] & [0] \\ [0] & \big(E/2(1+v)\big)[\overline{Q}] \end{bmatrix}, \tag{47}$$

where $\left[\hat{D}^{alg}\right]$ is the consistent tangent in principal form, from (34), and $[\overline{Q}]$ given by [5], was shown in [7] to be

$$[\overline{Q}] = \begin{bmatrix} \frac{\sigma_1-\sigma_2}{\sigma_{t_1}-\sigma_{t_2}} & 0 & 0 \\ 0 & \frac{\sigma_2-\sigma_3}{\sigma_{t_2}-\sigma_{t_3}} & 0 \\ 0 & 0 & \frac{\sigma_1-\sigma_3}{\sigma_{t_1}-\sigma_{t_3}} \end{bmatrix}. \tag{48}$$

4 Modified Reuleaux tension cut-off

By introducing the additional yield criterion and plastic potential

$$f_c = \rho - \alpha_c\overline{\rho}(\xi-\xi_{co}) \qquad \text{and} \qquad g_c = \rho - \beta_c\overline{\rho}(\xi-\xi_{cg}), \tag{49}$$

we modify the NAF MR cone to include a tension cut-off, where (i) $\alpha_c \in [-1,\alpha]$ and $\beta_c \in [\alpha_c, 0]$ are the opening angles of the yield and plastic potential surfaces, and (ii) ξ_{co} and ξ_{cg} are the intersections of the yield and plastic potential surfaces with the hydrostatic axis. With this MR cut-off, the intersection between the two surfaces lies in a single deviatoric plane, given by

$$\xi_j = \frac{\alpha_c\xi_{co} - \alpha\xi_c}{\alpha_c - \alpha}. \tag{50}$$

Consider the trial elastic stress $\{\sigma_t\}$ (given by a trial elastic strain $\{\varepsilon_t^{\mathrm{e}}\}$) lying outside the yield surface ($f>0$ or $f_c>0$). For this state there are seven distinct stress return regions associated with the tension cut-off MR cone, as shown in Figure 5:

		ξ_{cp}	θ_{cp}
A_{co}	Return to the cut-off apex (point)	ξ_{co}	–
A_j	Return to the yield surface intersection on the compression meridian (point)	ξ_j	$\pi/6$
B_{mp}	Return to the main yield surface compression meridian (line)	$<\xi_j$	$\pi/6$
B_{co}	Return to the cut-off yield surface compression meridian (line)	$>\xi_j$	$\pi/6$
B_j	Return to the yield surface intersection (arc)	ξ_j	$<\pi/6$
C_{co}	Return to the cut-off non-planar surface	$>\xi_j$	$<\pi/6$
C_{mp}	Return to the main yield non-planar surface	$<\xi_j$	$<\pi/6$

Return regions B_{mp} and C_{mp} have been dealt with in sections 3.4 and 3.3, respectively. A_{co}, B_{co} and C_{co} are covered by Sections 3.4, 3.3 and 3.2 with $\alpha=\alpha_c$, $\beta=\beta_c$ and hydrostatically shifting the trial stress state such that the cut-off yield surface intersects with the stress origin. Returns A_j and B_j are considered in Section 4.1.

To determine the return location of a trial point outside the yield surface, a three-stage process may be required. We initially make use of an apex boundary surface

$$^{\varsigma}f_{ap} = {}^{\varsigma}\rho + \frac{1}{{}^{\varsigma}\beta_c\overline{\rho}}({}^{\varsigma}\xi - {}^{\varsigma}\xi_{co}). \tag{51}$$

Trial states with ${}^{\varsigma}f_{ap} \leq 0$ will return to the apex of the cut-off with $\{\sigma\} = (\xi_{co}/\sqrt{3})\{1\}$. For this case the consistent tangent is given by (11). For points outside the apex boundary surface (${}^{\varsigma}f_{ap} > 0$) the return hydrostatic stress, ${}^{\varsigma}\xi_{cp}$, is calculated from (29), assuming that the point returns to the main yield surface. If ${}^{\varsigma}\xi_{cp} < {}^{\varsigma}\xi_j$ then one continues with the procedure outlined in Figure 4 (from the third point of step 1.(e).iv. onwards), otherwise return the trial point onto the cut-off yield surface. Once the return hydrostatic stress on the cut-off surface has been calculated, it is necessary to check if ${}^{\varsigma}\xi_{cp} > {}^{\varsigma}\xi_j$. If it is, then one continues with the stress return (again from the third point of step 1.(e).iv. Figure 4, onwards). Otherwise the trial stress will return to the intersection between the two yield surfaces (described below).

4.1 Interface return

The junction locus, between the main yield surface and the cut-off cone, lies in a single deviatoric plane where $\xi = \xi_j$, given by (50). The return stress for a trial point in this return region can be calculated using the following procedure.

1. Set ${}^{\varsigma}\xi_{cp} = {}^{\varsigma}\xi_j$,
2. Calculate ϕ_{cp} from (30),
3. Find ${}^{\varsigma}\rho_{cp} = {}^{\varsigma}\alpha\overline{\rho}(\theta){}^{\varsigma}\xi_{cp}$, using $\overline{\rho}(\theta)$ from (2),
4. θ_{cp} may then be determined from (31),
   (a) if $\theta_{cp} < \pi/6$, then return to the intersection arc, B_j,
   (b) if $\theta_{cp} \geq \pi/6$, then return to the intersection point on the compression meridian, A_j

$$\theta_{cp} = \pi/6, \qquad {}^{\varsigma}\rho_{cp} = {}^{\varsigma}\alpha({}^{\varsigma}\xi_{cp} - {}^{\varsigma}\xi_c) = {}^{\varsigma}\alpha_c({}^{\varsigma}\xi_{cp} - {}^{\varsigma}\xi_{co}).$$

5. Subsequently ${}^{\varsigma}\xi_{cp}$ and ${}^{\varsigma}\rho_{cp}$ can transformed back into conventional stress space to calculate the final return stress $\{\sigma_{cp}\}$ using the Haigh-Westergaard expression (17).

The complete numerical procedure for the combined non-associated flow, tension cut-off modified Reuleaux cone is given in Figure 6.

4.1.1 Interface consistent tangent

In order to define the consistent tangent for the interface return, we require an equation for the tangent of the intersection arc between the main MR yield surface and the MR cut-off. On this arc (B_j) the deviatoric normal to the yield and plastic potential surfaces coincide for both manifolds. The direction of the interface arc $\{r_j\}$, orthogonal to both the deviatoric normal to the yield surface and the hydrostatic axis (see Figure 5) is given by

$$\{r_j\} = \{f_{,\sigma}^{dev}\} \times \{1\}, \tag{52}$$

where $\times$ denotes the vector cross product and $\{f_{,\sigma}^{dev}\}$ is given by (38). Thus $\{r_j\}$ is given by

$$\{r_j\} = \{f_{,\sigma_2}^{dev} - f_{,\sigma_3}^{dev} \qquad f_{,\sigma_3}^{dev} - f_{,\sigma_1}^{dev} \qquad f_{,\sigma_1}^{dev} - f_{,\sigma_2}^{dev}\}^T. \tag{53}$$

The 3×3 elasto-plastic tangent matrix (in principal form) is subsequently given by

$$\left[\hat{D}^{ep}\right] = \frac{\{r_j\}\{r_j\}^T}{\{r_j\}^T\left[\hat{C}^{\mathrm{e}}\right]\{r_j\}}, \tag{54}$$

where $\left[\hat{C}^{\mathrm{e}}\right]$ is the 3×3 (principal) elastic compliance matrix. Calculation of the consistent elasto-plastic tangent requires determination of the plastic multipliers associated with the active yield surfaces; namely the main yield surface and the cut-off yield surface. Using Koiter's rule [15], the plastic strain associated with a return onto the interface arc is given by

$$\{\Delta\varepsilon^{\mathrm{p}}\} = \Delta\gamma\{g_{,\sigma}\} + \Delta\gamma_c\{g_{c,\sigma}\}, \tag{55}$$

where $\Delta\gamma$ and $\Delta\gamma_c$ are the incremental plastic multipliers and $\{g_{,\sigma}\}$ and $\{g_{c,\sigma}\}$ are the derivatives of the plastic potentials for the main and cut-off yield surfaces respectively. The increment in the plastic strain is given by

$$\{\Delta\varepsilon^{\mathrm{p}}\} = \{\varepsilon_t^{\mathrm{e}}\} - \{\varepsilon_{cp}^{\mathrm{e}}\}, \tag{56}$$

where $\{\varepsilon_t^{\mathrm{e}}\}$ and $\{\varepsilon_{cp}^{\mathrm{e}}\}$ are the elastic trial and return strains, respectively. The plastic multipliers can be calculated by substituting (56) into (55) and rearranging to obtain

$$\Delta\gamma_c = \frac{(\Delta\varepsilon_1^{\mathrm{p}})(g_{,\sigma_3}) - (\Delta\varepsilon_3^{\mathrm{p}})(g_{,\sigma_1})}{(g_{,\sigma_3})(g_{c,\sigma_1}) - (g_{c,\sigma_3})(g_{,\sigma_1})} \qquad \text{and} \qquad \Delta\gamma = \frac{\Delta\varepsilon_1^{\mathrm{p}} - (\Delta\gamma_c)(g_{c,\sigma_1})}{g_{,\sigma_1}}. \tag{57}$$

These plastic multipliers are subsequently used to calculate the principal consistent tangent matrix

$$\left[\hat{D^{alg}}\right] = \frac{\{r_j\}\{r_j\}^T}{\{r_j\}^T\left[\hat{C}^{\mathrm{e}}\right]\left[Q_j\right]\{r_j\}}, \tag{58}$$

where

$$\left[Q_j\right] = [1] + \Delta\gamma[\hat{C}^{\mathrm{e}}]^{-1}[g_{,\sigma\sigma}] + \Delta\gamma_c[\hat{C}^{\mathrm{e}}]^{-1}[g_{c,\sigma\sigma}]. \tag{59}$$

The 6×6 consistent tangent matrix is then given by

$$\left[D^{alg}\right] = \begin{bmatrix} \left[\hat{D}^{alg}\right] & [0] \\ [0] & (E/2(1+v))\left[\overline{Q}\right] \end{bmatrix}, \tag{60}$$

where $[\overline{Q}]$ is calculated from (48).

4.1.2 Interface corner consistent tangent

As Clausen *et al.* have shown [5], the elasto-plastic consistent tangent for the intersection of three yield planes is simply

$$\left[D^{alg}\right] = \begin{bmatrix} [0] & [0] \\ [0] & (E/2(1+v))\left[\overline{Q}\right] \end{bmatrix}, \tag{61}$$

where $[\overline{Q}]$, in this case, is given by (24). Recall that in all cases, the consistent tangent matrices (11), (25), (47), (60) and (61) need to be transformed back to their generalised form using the eigenvectors of the trial elastic strain (see Clausen *et al.* [5]).

5 Finite deformation framework

This paper uses an updated Lagrangian framework to account for geometric non-linearities inherent in large strain analysis. Note that a number of the earlier updated formulations were approximate in that they were restricted to small elastic strains [2]. This restriction does not hold here. In this paper the term *updated Lagrangian* refers to the strategy used by Holzapfel [12] and Bathe [1], where the linearisation of the internal virtual work is performed in the current configuration using the spatial derivatives. For more details see [1, 10], amongst others. In this framework all static and kinematic variables are referred to the previously converged state. The deformation gradient provides the fundamental link between the current and the reference configurations

$$[F] = \left[\frac{\partial\{x\}}{\partial\{X\}}\right] = \left[[1] + \frac{\partial\{u\}}{\partial\{X\}}\right], \tag{62}$$

where $\{x\}$ and $\{X\}$ are the coordinates of the same point in the current and reference configurations, respectively. $\{u\}$ is the displacement between the configurations. The multiplicative *Lee decomposition* of $[F]$, initially proposed by [16, 17], into elastic $[F^{\mathrm{e}}]$ and plastic $[F^{\mathrm{p}}]$ deformation gradients is given by

$$[F] = [F^{\mathrm{e}}][F^{\mathrm{p}}]. \tag{63}$$

This decomposition is a fundamental assumption of the adopted framework.

Within a finite deformation framework there exist choices for the stress and strain measures. Certain combinations provide advantages when moving between infinitesimal and large strain theories. Here we use a logarithmic strain–Kirchhoff stress relationship in conjunction with an implicit exponential map for the plastic flow equation to allow the implementation of standard small strain constitutive algorithms within a finite deformation framework without modification. See [10], amongst others, for more details on the recovery of the infinitesimal format of the stress return algorithms. It is one of the most successful and straight-forward ways of implementing large strain elasto-plasticity [14]. The logarithmic strain is defined as

$$[\varepsilon] = \ln[v] = \frac{1}{2}\ln[b], \tag{64}$$

where $[v]$ and $[b]$ are the left stretch and left Cauchy-Green strain matrices, respectively. The logarithm of $[v]$ or $[b]$ is obtained using spectral decomposition into principal values (see [25] for details) and using the inverse decomposition to recover the full six component symmetric matrix. $[v]$ is obtained from the polar decomposition of the deformation gradient, defined as the symmetric component of $[F]$, given by $[v] = \sqrt{[b]} = \sqrt{[F][F]^T}$. The Kirchhoff stress, $\{\tau\}$ is defined as

$$\{\tau\} = J\{\sigma\}, \tag{65}$$

where J, the volume ratio, is the determinant of the deformation gradient and $\{\sigma\}$ is the true (or Cauchy) stress. An isotropic small strain constitutive model can be incorporated within this framework without modification. An elastic logarithmic trial strain, $\{\varepsilon_t^{\mathrm{e}}\}$, is calculated from the trial elastic deformation gradient and used as the input into the constitutive model (along with any internal variables). The model will return the updated elastic logarithmic strain $\{\varepsilon^{\mathrm{e}}\}$, internal variables and the Kirchhoff stress $\{\tau\}$, from which the Cauchy stress can subsequently be calculated from (65). The constitutive model simply supplies the small strain algorithmic tangent stiffness matrix $\left[D^{alg}\right] = \left[\partial\tau/\partial\varepsilon_t^{\mathrm{e}}\right]$. This tangent is no longer consistent with the global finite-element procedure. Instead we use the the consistent spatial tangent modulus, written here in subscript notation

$$a_{ijkl} = \frac{1}{2J} D^{alg}_{ijmn} L_{mnpq} B^{a}_{pqkl} - S_{ijkl}, \tag{66}$$

where

$$L_{mnpq} = \frac{\partial \ln(b_t^{\mathrm{e}})_{mn}}{\partial (b_t^{\mathrm{e}})_{pq}}, \qquad B^{a}_{pqkl} = \delta_{pk}(b_t^{\mathrm{e}})_{ql} + \delta_{qk}(b_t^{\mathrm{e}})_{pl}, \qquad S_{ijkl} = \sigma_{il}\delta_{jk}. \tag{67}$$

D^{alg}_{ijmn} is the consistent tangent from the *unmodified* small strain constitutive model and $(b_t^{\mathrm{e}})_{mn}$ is the elastic trial left Cauchy-Green strain tensor. L_{mnpq} is determined as a particular case of the derivative of a general symmetric second order tensor function with respect to its argument[1]. This framework was first described by de Souza Neto and Perić [9] who demonstrated the importance of using the exact derivatives of the tensor quantities by making comparisons with the approximate derivatives through convergence analysis. The element stiffness matrix is obtained from

$$[k^e] = \sum_{i=1}^{n_{gp}} [G_i]^T [a_i][G_i] \big| [J_i] \big| w_i \tag{68}$$

where $[a_i]$, from (66), is now written in matrix form and n_{gp} gives the number of Gauss points. $[G_i]$ is the (9-component) strain-displacement matrix, $[J_i]$ is the Jacobian matrix obtained from the derivatives of the shape functions and the updated nodal coordinates and w_i is the weight function. The element internal forces are calculated in a manner analogous to infinitesimal theory.

The following points summarise the modifications required for an infinitesimal linear elastic finite-element code in order to implement the updated Lagrangian large strain formulation.

1. The primary internal variable is the deformation gradient, $[F]$.
2. The derivatives of the shape functions are calculated with respect to the updated nodal coordinates.
3. The non–symmetric material spatial tangent modulus, $[a]$, and the full (9-component) strain-displacement matrix, $[G]$, are used to form the element stiffness matrix.
4. An inelastic constitutive model is included.
5. The global equilibrium equation is solved using the Newton-Raphson (N-R) scheme.

6 Numerical analysis

6.1 Stress return error analysis

The accuracy of the stress return algorithm was assessed for $1 \leq \rho_t/(\alpha\overline{\rho}(\theta_t)\xi_t) \leq 6$ and $-\pi/6 \leq \theta_t \leq \pi/6$. A Young's modulus of 100MPa and a Poisson's ratio of 0.2 were used for the material's elastic properties. $\psi_{MC} = \pi/9$, $\psi_g = \pi/18$ and $\overline{\rho}_e = 0.8$ define the MR cone. A hydrostatic pressure of $\xi_t = -1$MPa was used for all of the elastic trial stresses. In this material point analysis, the starting stress state was located on the yield

[1] Traditionally the derivative of a tensor function with respect to its argument has been solved by considering the spectral decomposition of the tensor function and using the product rule to obtain the derivative. However, calculation of the derivative in the case of repeated eigenvalues requires the use of eigen–projections to overcome the non-uniqueness of the eigenvalues, a result originally obtained by Carlson and Hoger [4]. Miehe [18] subsequently presented two methods for the calculation of the derivative of a symmetric second order tensor with respect to is argument.

surface at the shear meridian ($\theta = 0$). The constitutive model was then subjected to an elastic strain increment corresponding to the elastic trial stress state, see Figure 7(ii). The return stress from this single strain increment was compared with the solution obtained by splitting the strain increment into 10,000 sub-increments.

The following error measure was used to assess the accuracy of the stress return algorithm

$$e = \frac{\sqrt{\Big\{\{\sigma_{cp}\} - \{\sigma_e\}\Big\}^T \Big\{\{\sigma_{cp}\} - \{\sigma_e\}\Big\}}}{\sqrt{\{\sigma_e\}^T\{\sigma_e\}}}, \tag{69}$$

where the sub-incremented solution, $\{\sigma_e\}$, is treated as the *exact* stress return and $\{\sigma_{cp}\}$ is the one-step analytical return. A stress iso-error map is given in Figure 7(i). This analysis revealed a maximum error of 3.62%, corresponding to a trial stress on the extension meridian ($\theta = -\pi/6$) at $\rho_t/(\alpha\overline{\rho}\xi_t) = 4.1$. Zero error appears along the locus $\theta_t = 0$, $\rho_t/(\alpha\overline{\rho}\xi_t) = 1$ to $\theta_t \to -0.2160$, $\rho_t/(\alpha\overline{\rho}\xi_t) \to \infty$. Much of the trial area has an error of less than 0.5%. Larger errors are associated with trial stresses near the extension meridian and in the vicinity of the compression meridian return region. These are due to the increased tangential component of the trial stress increment. The errors follow the same general pattern as reported for the associated Reuleaux plasticity model by Coombs *et al.* [7]. The maximum error has increased from 2.56% due to the non-associated flow rule increasing the length of the integrated stress return.

Figure 8 demonstrates the stress return algorithm when the applied strain increment changes the ordering of the principal stress between the original (or previously converged) and trial stress state. This analysis was conducted with the same material parameters as above except that $\psi_g = 0$ and the cohesion $c = 100$kPa , allowing the stress return to be visualised in the π-plane. The initial stress state $\{\sigma_n\}$ was located at the intersection of the shear meridian with the yield surface. An unordered principal strain increment of $\{\Delta\varepsilon\} = \{-1.6131 \quad 1.8065 \quad -0.1934\}^T \times 10^{-3}$ was applied in a single step and also in two specifically selected steps, where the strain increment was split such that (i) the first increment locates the trial stress $\{\sigma_{t_1}\}$ on the boundary of the region that will result in a corner return and (ii) the second increment supplies the remainder of the total strain increment. Figure 8 (i) demonstrates the stress return in principal stress space where the components (σ_x, σ_y, σ_z) are not associated with any particular ordering. That is, σ_x (and σ_y or σ_z) may be the major, intermediate or minor principal stress. In this way, stress points can exist in all six sextants of the pi-plane. Hereafter we refer to this as true stress space. Figure 8 (ii) illustrates the processes in principal stress space where the ordering $\sigma_1 \le \sigma_2 \le \sigma_2$ holds. When an applied strain increment changes the ordering of the principal stresses such that the stress path moves through a corner return region there will be an additional error associated with the stress return. In true stress space, applying the strain increment in a single step results in a trial stress state $\{\sigma_t\}$ in the sextant where $\sigma_x \le \sigma_z \le \sigma_y$. This trial state will return onto the yield surface at $\{\sigma_{cp}\}$. In the ordered principal stress space the trial point is again located at $\{\sigma_t\}$. This principal trial will return to $\{\sigma_{cp}\}$ which (for this case) coincides with the same return stress in true stress space. When the strain increment is split into two components, the first trial $\{\sigma_{t_1}\}$ returns onto the corner of the yield surface $\{\sigma_{cp}\}$ while the remainder of the increment results in the trial $\{\sigma_{t_2}\}$ which returns to $\{\sigma_{cp_2}\}$. Viewing this two-step process in principal stress space, the initial increment is identical to that in true stress space. The second increment is mirrored about the $\sigma_z = \sigma_y$ axis so that it remains in the $\sigma_1 \le \sigma_2 \le \sigma_2$ sextant. Once the return is formed in principal stress space, it is then transformed back into true stress space. For the case demonstrated, the relative error (using (69) with $\{\sigma_e\}$ taken as $\{\sigma_{cp_2}\}$) between the single step and the two step return is 10.27%. The *absolute* error when the strain increment is split into 10,000 subincrements is 12.56%. This type of error is not unique to the modified Reuleaux constitutive model; it will be present for any yield surface with corners, such as the widely used Tresca and Mohr-Coulomb models.

6.2 Run time analysis

The run time of the single-step analytical BE return is compared with a conventional iterative BE stress return in Figure 9. The analysis considered trial stresses between $1 \le \rho_t/(\alpha\overline{\rho}\xi_t) \le 6$ and $-\pi/6 \le \theta_t \le \pi/6$. A Young's modulus of 100MPa and a Poisson's ratio of 0.2 were again used for the material's elastic properties. Similarly, $\psi_{MC} = \pi/9$, $\psi_g = \pi/18$ and $\overline{\rho}_e = 0.8$ define the MR cone and a hydrostatic pressure of $\xi_t = -1$MPa was used for all of the elastic trial stresses. The constitutive model was then subjected to a strain increment corresponding to the elastic trial stress state, see Figure 9(ii). When returning to the corner or the apex, both the approaches (analytical and numerical BE) use the same single-step return discussed in the preceding sections. However, when returning onto the non-planar surface, the conventional (numerical) BE method requires multiple local iterations to obtain convergence. The number of iterations and the ratio of the numerical to analytical BE run times are presented in Figure 9(i). The analytical return demonstrates a 2-4 times speed-up over the iterative numerical method (for the considered trial stress states). The increase in time required for the iterative approach is due, in part, to repeatedly calculating the first and second derivatives of the yield function with respect to stress. The non-smooth (stepped) region close to $\theta_t = \pi/12$ is a consequence of the finite grid size either side of the return region B-C boundary.

Note that although the same general trends are observed as for the associated case reported by Coombs *et al.* [7], a different form of the yield function, f, is used in this paper. Both yield functions describe the same yield surface, but they have different f fields outside the yield surface which can significantly affect the rate of converegence of an iterative backward Euler stress return. As a result, the maximum number of iterations for the NAF iterative return to converge (to the same tolerance) was reduced from 7, for the case of associated flow in [7], to 5.

6.3 Cylindrical expansion

In this section we present the analysis of the expansion of a thick-walled soil cylinder under internal pressure. This is a one-dimensional axi-symmetric problem but here we use a 2D version of our 3D FE code and make comparisons with the analytical solution provided by [28]. 3° of a cylinder with an initial internal radius (a_0) of 1m and an external radius (b_0) of 500m was discretised using one hundred four-noded plain strain quadrilateral elements with the length of the elements progressively increasing by a factor 1.2 from the inner to the outer surface. The following material parameters were used: Young's modulus of 100MPa, Poisson's ratio of 0.3, cohesion c of 70kPa, friction angle of 20° and $\overline{\rho}_e = 0.8$ (to coincide with $\overline{\rho}_e$ for M-C). The internal radius was expanded to 5m via 400 equal displacement-controlled increments. Figure 10 presents the pressure-internal expansion plots for the four associated flow perfect plasticity constitutive models: D-P, M-C, Willam-Warnke (W-W) [26] cone and MR. a/a_0 is the ratio of the current to the original internal radius. The M-C numerical solution displays excellent agreement with the analytical solution. Results for the MR cone using $\overline{\rho}_e = 0.5001$ and $\overline{\rho}_e = 0.9999$ demonstrate the model's ability to provide solutions spanning between those provided by the M-C and D-P cones. With $\overline{\rho}_e = 0.8$ the W-W and MR cones produced a stiffer response when compared against the M-C solution.

Table 1 gives run time comparisons between the different constitutive models. $\sum(\mathrm{NR}_{it})$ is the total number of global N-R iterations, $\max(\mathrm{NR}_{it})$ is the maximum number of N-R iterations for any loadstep, t/t_{M-C} is the run time normalised with respect to the M-C run time. The W-W formulation, which produced similar results to the MR cone, required a 58.9% increase in the run-time. Whereas the MR solution gave a run time which was only 7.7% greater than M-C.

6.4 Cavity expansion

In this section we present the analysis of the expansion of a cylindrical soil cavity under internal pressure. This also is a one-dimensional axi-symmetric problem but again we use our 2D FE code to make comparisons with an analytical solution. Only 3° of the cavity (with internal radius of 1m and fixed outer boundary of radius 2km) is discretised using one hundred and fifty four-noded plain strain quadrilateral elements (the size of the elements were progressively increased by a factor 1.1 from the inner to the outer surface). Identical material parameters as used in Section 6.3 were adopted. The internal radius was expanded to 5m via 80 equal displacement-controlled increments.

Figure 11 presents the pressure-internal radius plots for M-C and MR cones for a range of dilation angles. As with the cylinder expansion problem described above, the MR cone produces a stiffer response compared to M-C, for all examined dilation angles. The M-C numerical solution displays excellent agreement with the analytical solution [27] for both associated and non-associated flow.

Reducing the dilation angle causes a progressive softening of the pressure-displacement response for the internal expansion problem. Reducing ψ_g from $\pi/9$ to 0 leads to a reduction of 45.3% and 40.5% of the maximum pressure for the MR and M-C models, respectively. This reduction in pressure is a consequence of the direction of plastic return onto the yield surfaces. As the dilation angle reduces, so does the volumetric component of the plastic stress corrector. This gives rise to the return stress state having a reduced hydrostatic (and deviatoric) stress when compared with the case of associated flow.

Figure 12 (i) and Table 2 present the convergence results for the cavity expansion problem for the MR cone with a dilation angle of $\psi_g = \pi/18$ for loadsteps 76–80. The following measure of *normalised* (residual) out of balance force

$$|\{f_r\}| = \frac{\sqrt{\Big\{\{f_{ext}\} - \{f_{int}\}\Big\}^T \Big\{\{f_{ext}\} - \{f_{int}\}\Big\}}}{\sqrt{\Big\{f_{ext}\Big\}^T \Big\{f_{ext}\Big\}}} \tag{70}$$

was used to assess convergence, where $\{f_{ext}\}$ and $\{f_{int}\}$ are the external and internal forces, respectively. Figure 12 and Table 2 demonstrate the asymptotic quadratic convergence of the global N-R procedure for the NAF MR cone model. The convergence rate is confirmed by Figure 12 (ii) which gives the norm of the out-of-balance force against the previous out-of-balance force for the final loadstep showing that the convergence is asymptotically approaching a quadratic rate.

6.5 Rigid footing

The ability of MR to interpolate between D-P and M-C for the small-strain analysis was demonstrated in [7] for a plane strain incremental finite-element analysis of a 1m wide rigid strip footing bearing onto a weightless soil. In that paper it was shown that the run time advantages of the MR cone over W-W cone are considerable. Here we present the effect of including finite deformations, NAF and a tension cut-off for the analysis of a rigid strip footing bearing onto a weightless soil.

Due to symmetry only one half of the problem was considered. The mesh had a depth and width of 8m. 400 eight-noded quadrilaterals, with reduced four-point quadrature, modelled the problem (see Figure 13). The following material parameters were used: a Young's modulus of 100MPa, Poisson's ratio of 0.3, cohesion, c, of 100kPa, friction angle of $\pi/9$ and $\overline{\rho}_e = 0.8$. The problem was analysed for a surface displacement of 100mm applied using 100 equal displacement increments. An associated flow ($\psi_g = \pi/9$) and non-associated flow ($\psi_g = \pi/18$) MR cone (with and without a tension cut-off) were used in the analysis. The opening angle of the associated flow cut-off was set to $\alpha_c = \beta_c = -\tan(2\pi/9)$ with a hydrostatic interface (or junction) stress of $\xi_j = -200$kPa.

The normalised pressure-displacement relationship for the six cases, and for a Mohr-Coulomb constitutive model, are shown in Figure 14. Similar to the cavity expansion analysis, the non-associated flow model produces a softer response compared to the associated flow case. As expected, at small displacements the results for small strain and finite deformation are similar. The results deviate in the higher displacement range (> 60mm); with the finite deformation results producing stiffer responses. This progressive increase in stiffness is a consequence of the change in the nodal positions as the deformation proceeds. In this example, the pressure-displacement response of the cut-off non-associated MR cone was similar to that of the non-associated model without the cut-off.

Figure 15 presents the displaced surface profiles for three of the MR constitutive models (small strain AF, finite deformation NAF and NAF with cut-off). Local heave is significantly reduced using a non-associated flow rule for both the small strain and finite deformation analysis. The effect of finite deformation is to reduce the heave in the region immediately adjacent to the footing but increase the heave further away from the footing. The cut-off model increased the local heave, compared to the non-associated model without the cut-off, due to the additional dilative plastic strains generated when the stresses return onto the cut-off surface.

The convergence of the finite deformation footing problem is demonstrated in Figure 16 for loadsteps 16, 32, 50, 83 and 98 for the modified Reuleaux model with a cut-off. The number of integration points which are deforming elasto-plastically on different regions of the yield surface are given above each plot. While the number of integration points with stress states located on the cut-off increases with the displacement, the majority of the stress states fall on the non-planar surface of the main MR cone. The five plots demonstrate the convergence properties using the spatial consistent tangent. Although for some of the loadsteps the initial convergence rate is sub-optimal, the algorithm rapidly converges once the correct descent path has been found. Note that the tangent used for the first Newton-Raphson iteration is provided by the initial elastic stiffness.

Figure 17 presents the incremental plastic strain contours for the final loadstep for all six MR cases. The effect of accounting for the change in geometry as the deformation proceeds is to increase the depth of the plastic zone and increase the size of the elastic wedge immediately below the footing. All cases exhibit the characteristic band of concentrated plastic straining between the displacing wedge and the surrounding soil. Rigid body motion of the region between the wedge and curved zone of intense plastic straining is more apparent in the finite deformation NAF solution than the small strain AF results. This is shown in Figure 18 where the incremental nodal displacement vectors for the final loadstep are presented.

7 Conclusions

It is widely accepted that associated frictional plasticity models overestimate the dilation seen in particulate media. This paper extends the concept of energy-mapped stress space to non-associated flow elasto-plasticity. Operating in this stress space allows the construction of an analytical backward Euler stress return to a volumetrically non-associated frictional plasticity model that incorporates dependence on both the Lode angle and the intermediate principal stress via a modified Reuleaux deviatoric section. The model provides exact stress integration when moving along the compression meridian, or remaining on the tensile apex. Relatively small errors may be incurred when crossing the boundaries, or returning onto the non-planar yield surface (see Figure 7). The analytical return requires only a single step procedure, resulting in a robust algorithm for all stress return regions. This formulation provides considerable speed gains over the conventional iterative backward Euler method (see Figure 9).

The non-associated flow frictional perfect plasticity model was further extended by introducing an additional modified Reuleaux cone providing a cut-off to the main yield surface. Stress returns and consistent tangents for the seven possible regions (see Figure 5) have been fully defined. These constitutive models were incorporated within an logarithmic strain-Kirchhoff stress updated Lagrangian finite deformation framework that preserves

the stress return format of infinitesimal constitutive models.

Numerical examples have demonstrated the ability of the modified Reuleaux constitutive model to span between the results for Drucker-Prager and Mohr-Coulomb models (see Figure 10). The latter are two of the most widely used perfect plasticity models adopted in geomechanics. Unlike these M-C and D-P models, the MR formulation allows control of the shape of the deviatoric section independent of the friction (opening) angle of the yield surface. This feature offers a better fit to known experimental data than that provided by the M-C or D-P formulations.

The asymptotic quadratic convergence of the global Newton-Raphson procedure, in finite-element cylindrical cavity expansion simulations and a plane strain strip footing analysis demonstrated the value in constructing the consistent tangent for the new model. Run-time comparisons illustrated the computational advantage of the model over the more costly Willam-Warnke cone. The efficiency and increased realism of this NAF MR formulation demonstrates that it provides a valuable extension to the family of classical perfect plasticity models.

References

[1] K Bathe, *Finite Element Procedures*, Praentice-Hall, New Jersey, 1996.

[2] KJ Bathe, E Ramm and EL Wilson, *Finite element formulations for large deformation dynamic analysis*, Int. J. Numer. Meth. Engng. 9 (1975), 353–386.

[3] M Cai, *Influence of intermediate principal stress on rock fracturing and strength near excavation boundaries-Insight from numerical modeling*, Int. J. of Rock Mechanics and Mining Sciences 45 (2008), 763–772.

[4] DE Carlson and A Hoger, *The Derivative of a Tensor-valued Function of a Tensor*, Quart. Appl. Math. 44 (1986), 409–423.

[5] J Clausen, L Damkilde, and L Andersen, *Efficient return algorithms for associated plasticity with multiple yield planes*, Int. J. Numer. Meth. Engng. 66 (2006), 1036–1059.

[6] J Clausen, L Damkilde, and L Andersen, *An efficient return algorithm for non-associated plasticity with linear yield criteria in principal stress space*, Computers & Structures 85 (2007), 1795–1807.

[7] WM Coombs, RS Crouch and CE Augarde, *Reuleaux plasticity: Analytical backward Euler stress integration and consistent tangent*, Comput. Meth. Appl. Mech. Eng. 199 (2010), 1733–1743

[8] RS Crouch, H Askes, and T Li, *Analytical CPP in energy-mapped stress space: application to a modified Drucker-Prager yield surface*, Comput. Meth. Appl. Mech. Eng. 198 (5–8) (2009), 853–859.

[9] EA de Souza Neto and D Perić, *A computational framework for a class of fully coupled models for elasto-plastic damage at finite strains with reference to the linearization aspects*, Comput. Meth. Appl. Mech. Eng. 130 (1996), 179–193.

[10] EA de Souza Neto, D Perić, and DRJ Owen, *Computational methods for plasticity: Theory and applications*, John Wiley & Sons Ltd, 2008.

[11] E Fjær and H Ruistuen, *Impact of the intermediate principal stress on the strength of heterogeneous rock*, Journal of Geophysical Research 107 (2002).

[12] GA Holzapfel, *Nonlinear solid mechanics*, John Wiley & Sons Ltd. 2000.

[13] K Issen and V Challa, *Influence of the Intermediate Principal Stress on Compaction Localization Conditions*, The 41st U.S. Symposium on Rock Mechanics (USRMS), June 17–21, 2006.

[14] D-N Kim, FJ Montáns, and K-J Bathe, *Insight into a model for large strain anisotropic elasto-plasticity*, Comput. Mech. 44 (2009), 651–668.

[15] WT Koiter, *Stress-strain relations, uniqueness and varitional theorems for elastic-plastic materials with a singular yield surface*, Quart. Appl. Math., 11 (1953), 350–354.

[16] E Lee and D Lu, *Finite-Strain Elastic-Plastic Theory with Application to Plane-Wave Analysis*, J. App. Phys. 38 (1967), 19–27.

[17] E Lee, *Elastic-plastic deformation at finite strains*, J. App. Mech. 36 (1969), 1–6.

[18] C Miehe, *Comparison of two algorithms for the computation of fourth-order isotropic tensor functions*, Computers & Structures 66 (1998), 37–43.

[19] FC Moon, *Franz Reuleaux: Contributions to 19th C. kinematics and theory of machines*, Tech. report, Cornell Library Technical Reports and Papers, 2002.

[20] AP Morris and DA Ferrill, *The importance of the effective intermediate principal stress (σ'_2) to fault slip patterns*, Journal of Structural Geology 31 (2009), 950–959.

[21] F Reuleaux, *The kinematics of machinery: Outlines of a theory of machines*, Macmillan and Co., London, 1876.

[22] A Säyao and YP Vaid, *Effect of intermediate principal stress on the deformation response of sand*, Can. Geotech. J. 33 (1996), 822–828.

[23] JC Simo and TJR Hughes, *General return mapping algorithims for rate-independent plasticity*, Constitutive Laws for Engineering Materials: Theory and Applications, Cambridge University Press, 1987.

[24] JC Simo and TJR Hughes, *Computational inelasticity*, Springer, New York, 1998.

[25] A Spencer, *Continuum Mechanics*, Dover Publications, 1980.

[26] KJ Willam and EP Warnke, *Constitutive model for the triaxial behaviour of concrete*, Proceedings of the May 17-19 1974, International Association of Bridge and Structural Engineers Seminar on Concrete Structures Subjected to Triaxial Stresses, held at Bergamo Italy, 1974.

[27] HS Yu and GT Houlsby. *Finite cavity expansion in dilatant soils: Loading analysis*, Géotechnique 41, (1991), 173–183.

[28] HS Yu. *Expansion of a thick cylinder of soils*, Computers & Geotechnics 14 (1992), 21–41.

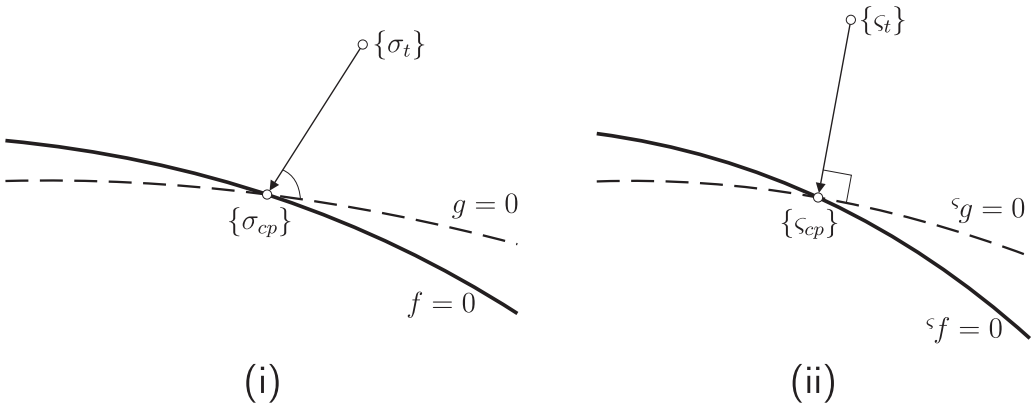

Figure 1: Closest point projection for NAF: (i) conventional stress space (ii) energy-mapped stress space.

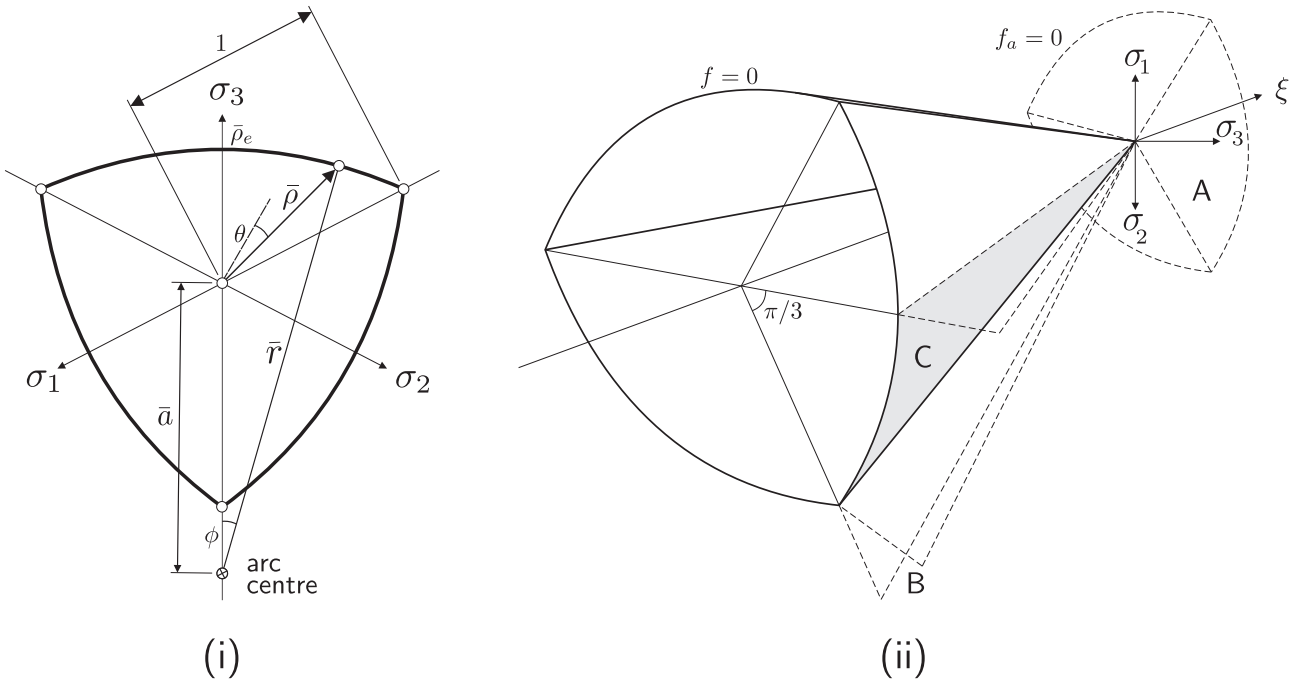

Figure 2: (i) Modified Reuleaux deviatoric section (ii) Modified Reuleaux yield surface cones showing the three stress return regions.

	M-C	D-P	MR	W-W
$\sum(\mathrm{NR}_{it})$	1166	1200	1200	1203
$\max(\mathrm{NR}_{it})$	3	3	3	6
$\mathrm{t/t_{M\text{-}C}}$	1	1.012	1.077	1.666

Table 1: Run time comparisons for the internal expansion of a thick-walled soil cylinder.

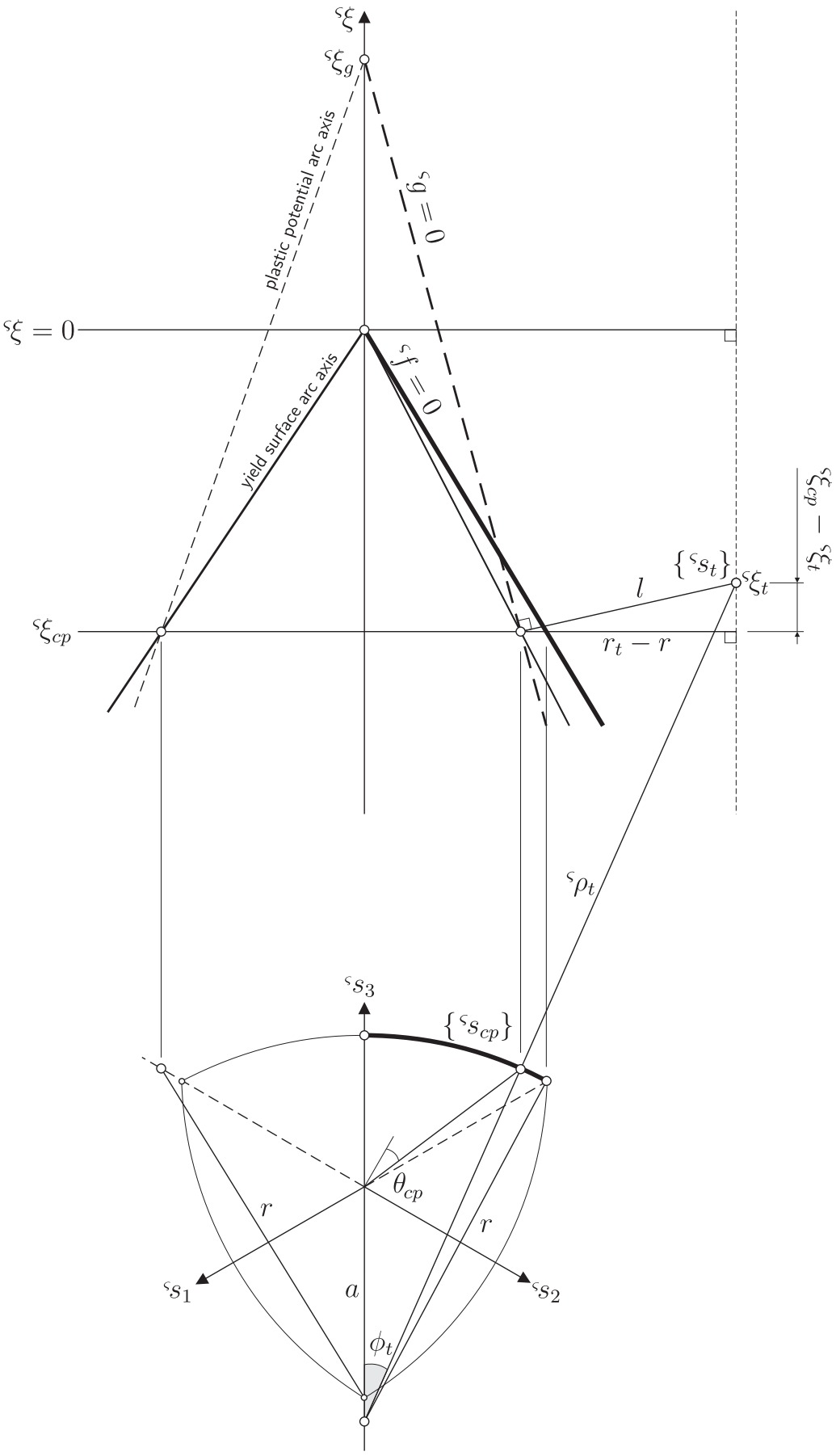

Figure 3: Geometric illustration of the solution in energy-mapped stress space $\{\varsigma\}$.

1. INPUT: $\{\varepsilon_t^{\mathrm{e}}\}$, v, E, α, β, ξ_c and $\overline{\rho}_e$
   (a) Transform the trial elastic strain $\{\varepsilon_t^{\mathrm{e}}\}$ into its principal components and store the associated eigenvectors.
   (b) Calculate the principal (elastic) trial stress $\{\sigma_t\} = [\hat{C}^{\mathrm{e}}]^{-1}\{\varepsilon_t^{\mathrm{e}}\}$.
   (c) Determine the value of the yield function f at the trial state (5).
   (d) IF $f < tol$
      i. Elastic response, $\{\sigma_{cp}\} = \{\sigma_t\}$, $\{\varepsilon_{cp}^{\mathrm{e}}\} = \{\varepsilon_t^{\mathrm{e}}\}$.
      ii. $[D^{alg}] = [C^{\mathrm{e}}]^{-1}$
   (e) ELSE
      i. Transform ξ_t and ρ_t into energy-mapped stress space and form $\{\varsigma_t\}$ using the Haigh-Westergaard expression (17), where ξ_t, ρ_t and $\{\varsigma_t\}$ replace ξ, ρ and $\{\sigma\}$.
      ii. Determine the value of the apex boundary function ${}^{\varsigma}f_a$ from (10).
      iii. IF ${}^{\varsigma}f_a < tol$
         - Apex return, $\{\sigma_{cp}\} = \xi_c/\sqrt{3}\{1\}$ and $\{\varepsilon_{cp}^{\mathrm{e}}\} = [\hat{C}^{\mathrm{e}}]\{\sigma_{cp}\}$.
         - $[D^{alg}] = [0]$ (11).
      iv. ELSE
         - Hydrostatically translate the trial stress point by ${}^{\varsigma}\xi_c$ so that the yield surface intersects with the stress origin.
         - Solve for ${}^{\varsigma}\xi_{cp}$ using (29).
         - Calculate θ_{cp} using (31).
         - IF $\theta_{cp} < \pi/6$
            – Surface return, calculate ${}^{\varsigma}\rho_{cp} = {}^{\varsigma}\alpha\overline{\rho}(\theta)\,{}^{\varsigma}\xi_{cp}$ using $\overline{\rho}(\theta)$ from (2).
            – Transform ${}^{\varsigma}\xi_{cp}$ and ${}^{\varsigma}\rho_{cp}$, in energy-mapped stress space, back to ξ_{cp} and ρ_{cp} in conventional stress space.
            – Calculate $\{\sigma_{cp}\}$ from the Haigh-Westergaard expression (17).
            – Determine the derivatives required in order to calculate $[D^{alg}]$ from (47).
         - ELSE
            – Line return, calculate ${}^{\varsigma}\xi_{cp}$ from (16).
            – Determine θ_{cp} and ${}^{\varsigma}\rho_{cp}$ from (12).
            – Transform ${}^{\varsigma}\xi_{cp}$ and ${}^{\varsigma}\rho_{cp}$, in energy-mapped stress space, back to ξ_{cp} and ρ_{cp} in conventional stress space.
            – Calculate $\{\sigma_{cp}\}$ from the Haigh-Westergaard expression (17).
            – Determine $[D^{alg}]$ from (25).
         - END IF
         - Hydrostatically translate $\{\sigma_{cp}\}$ by ξ_c to return the yield surface to its original position.
      v. END IF
   (f) END IF
   (g) Transform the principal components back to generalised space using the eigenvectors from the trial elastic strain stored at 1.(a).
2. OUTPUT: $\{\sigma_{cp}\}$, $\{\varepsilon_{cp}^{\mathrm{e}}\}$ and $[D^{alg}]$

Figure 4: NAF modified Reuleaux numerical procedure

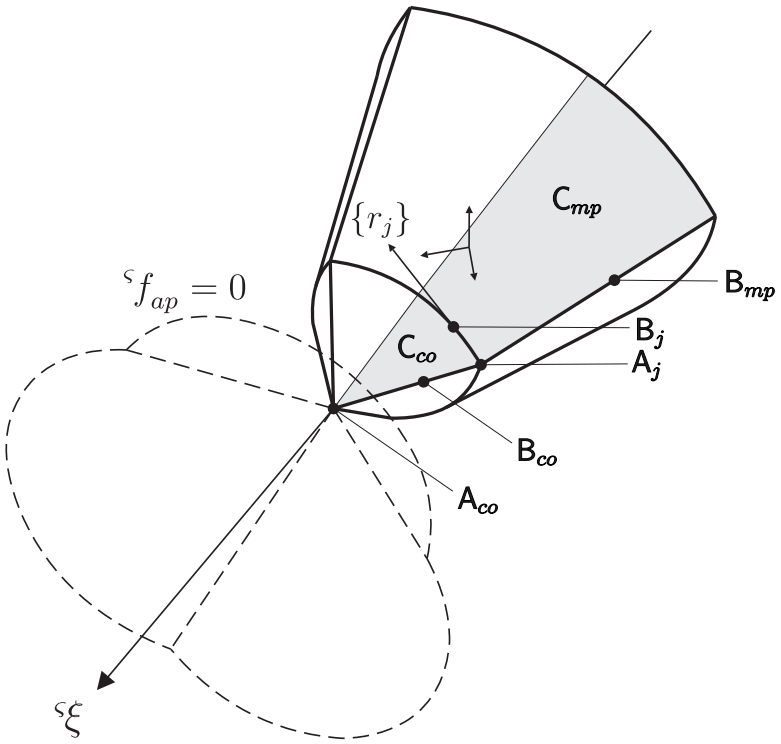

Figure 5: Seven stress return regions for the modified Reuleaux cut-off model.

Iteration	Loadstep				
	76	77	78	79	80
1	6.6987 E −01	6.7303 E −01	6.7599 E −01	6.7964 E −01	6.8322 E −01
2	1.0559 E −01	1.0690 E −01	1.0822 E −01	1.0971 E −01	1.1108 E −01
3	4.4568 E −03	4.5667 E −03	4.6846 E −03	4.8009 E −03	4.9183 E −03
4	1.1621 E −05	1.2187 E −05	1.2799 E −05	1.3417 E −05	1.4057 E −05
5	8.4626 E −11	9.7972 E −11	1.1991 E −10	1.1860 E −10	1.2274 E −10

Table 2: Internal expansion of a cylindrical cavity: Absolute residual out of balance force convergence for the NAF modified Reuleaux model.

1. INPUT: $\{\varepsilon_t^{\mathrm{e}}\}$, v, E, α, β, α_c, β_c, ξ_c, ξ_{co} (or ξ_j) and $\overline{\rho}_e$
   (a) Transform the trial elastic strain $\{\varepsilon_t^{\mathrm{e}}\}$ into its principal components.
   (b) Calculate the principal (elastic) trial stress $\{\sigma_t\} = [\hat{C}^{\mathrm{e}}]^{-1}\{\varepsilon_t^{\mathrm{e}}\}$.
   (c) Determine the value of the yield functions f (5) and f_c (49) at the trial state.
   (d) IF $f < tol$ AND $f_c < tol$
      i. Elastic response, $\{\sigma_{cp}\} = \{\sigma_t\}$, $\{\varepsilon_{cp}^{\mathrm{e}}\} = \{\varepsilon_t^{\mathrm{e}}\}$.
      ii. $[D^{alg}] = [C^{\mathrm{e}}]^{-1}$.
   (e) ELSE
      i. Transform ξ_t and ρ_t into energy-mapped stress space and form $\{\varsigma_t\}$ using the Haigh-Westergaard expression (17), where ξ_t, ρ_t and $\{\varsigma_t\}$ replace ξ, ρ and $\{\sigma\}$.
      ii. Determine the value of the boundary function ${}^{\varsigma}f'_{ap}$ from (51).
      iii. IF ${}^{\varsigma}f_{ap} < tol$
         - Cut-off apex return to A_{co}, $\{\sigma_{cp}\} = \xi_{co}/\sqrt{3}\{1\}$ and $\{\varepsilon_{cp}^{\mathrm{e}}\} = [\hat{C}^{\mathrm{e}}]\{\sigma_{cp}\}$.
         - $[D^{alg}] = [0]$ (11).
      iv. ELSE
         - Assuming that the trial stress returns to the main yield surface, calculate ξ_{cp} using (29) with parameters associated with the main plane.
         - IF $\xi_{cp} > \xi_j$
            – Assuming that the trial stress returns to the cut-off yield surface, calculate ξ_{cp} using (29) with parameters associated with the cut-off.
            – IF $\xi_{cp} < \xi_j$
            Interface return, follow the procedure outline in Section 4.1.
            – ELSE
            Cut-off return, follow the procedure outlined in Figure 4 point (e).iv. using parameters associated with the cut-off.
            – END IF
         - ELSE
            – Main yield surface return, follow the procedure outlined in Figure 4 point (e).iv. using parameters associated with the main plane.
         - END IF
      v. END IF
   (f) END IF
   (g) Transform the principal components back to generalised space using the eigenvectors from the trial elastic strain.
2. OUTPUT: $\{\sigma_{cp}\}$, $\{\varepsilon_{cp}^{\mathrm{e}}\}$ and $[D^{alg}]$

Figure 6: NAF modified Reuleaux with cut-off numerical procedure

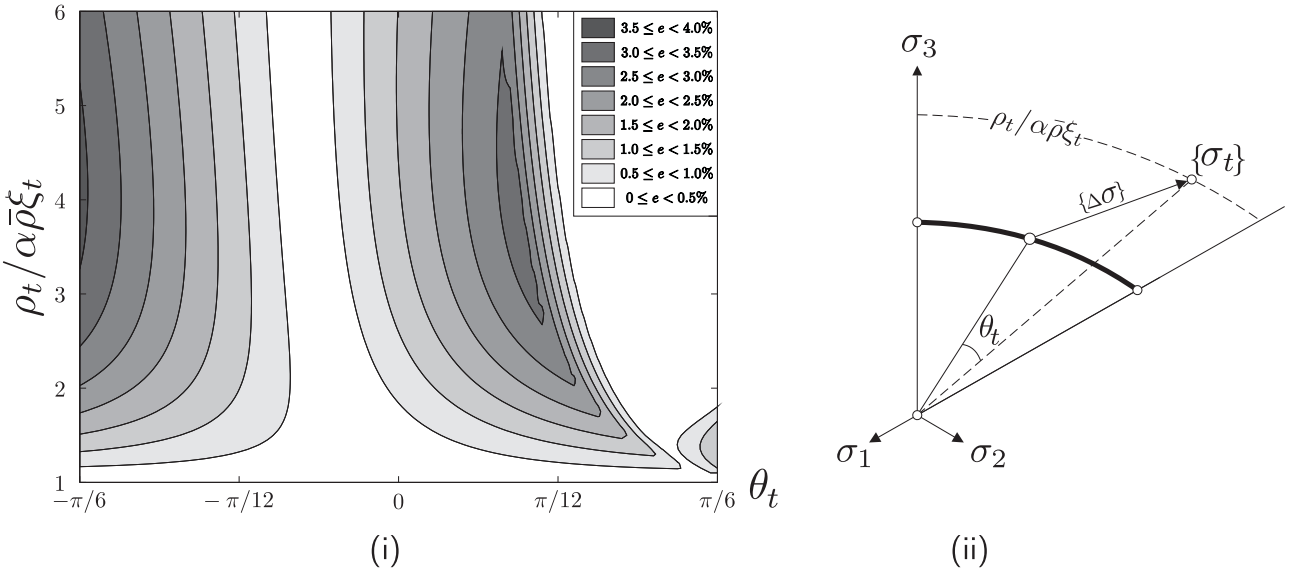

Figure 7: (i) Errors following from the single-step analytical backward Euler stress return (ii) geometric interpretation of a trial point in the error analysis.

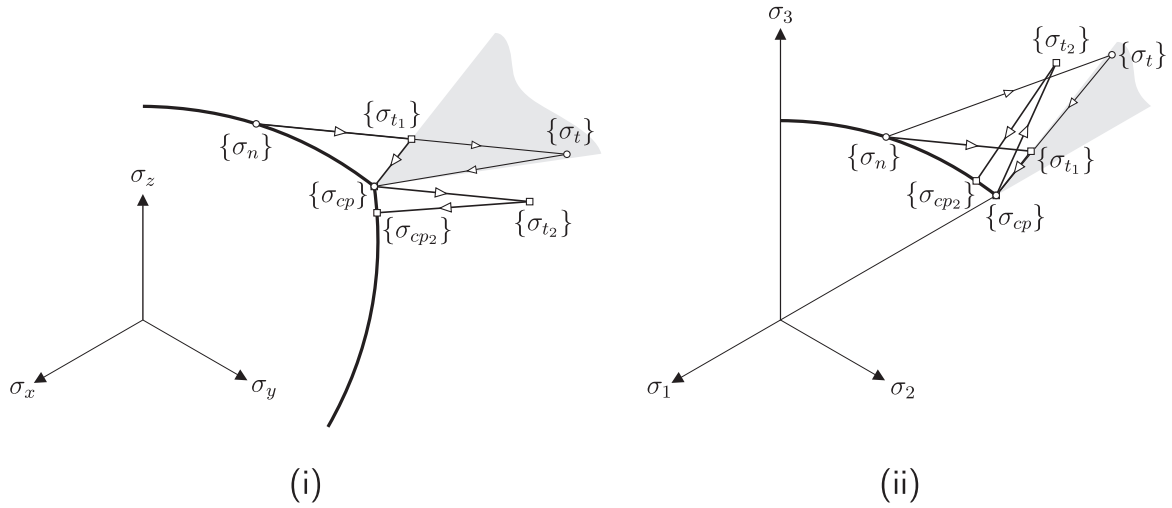

Figure 8: Modified reuleaux stress return crossing a corner. The figures illustrate a comparison between a single step and two specifically selected increments in (i) true stress space (ii) ordered principal stress space.

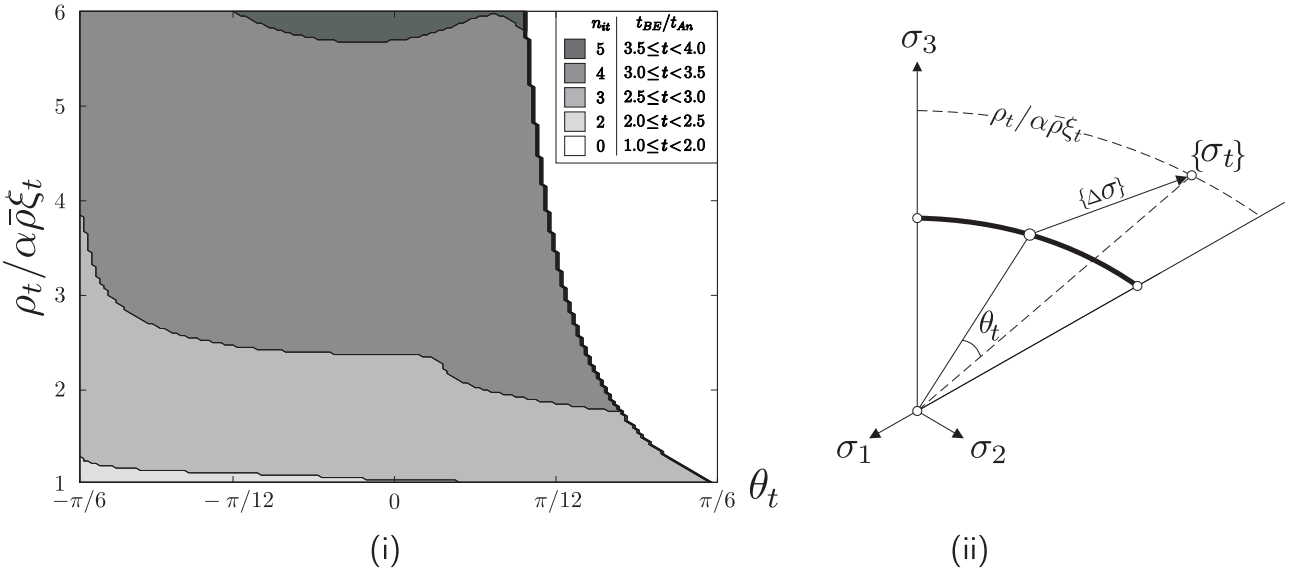

Figure 9: (i) Run time comparisons between conventional iterative backward Euler and the single-step analytical backward Euler stress returns (ii) geometric interpretation of a trial point in the run time analysis.

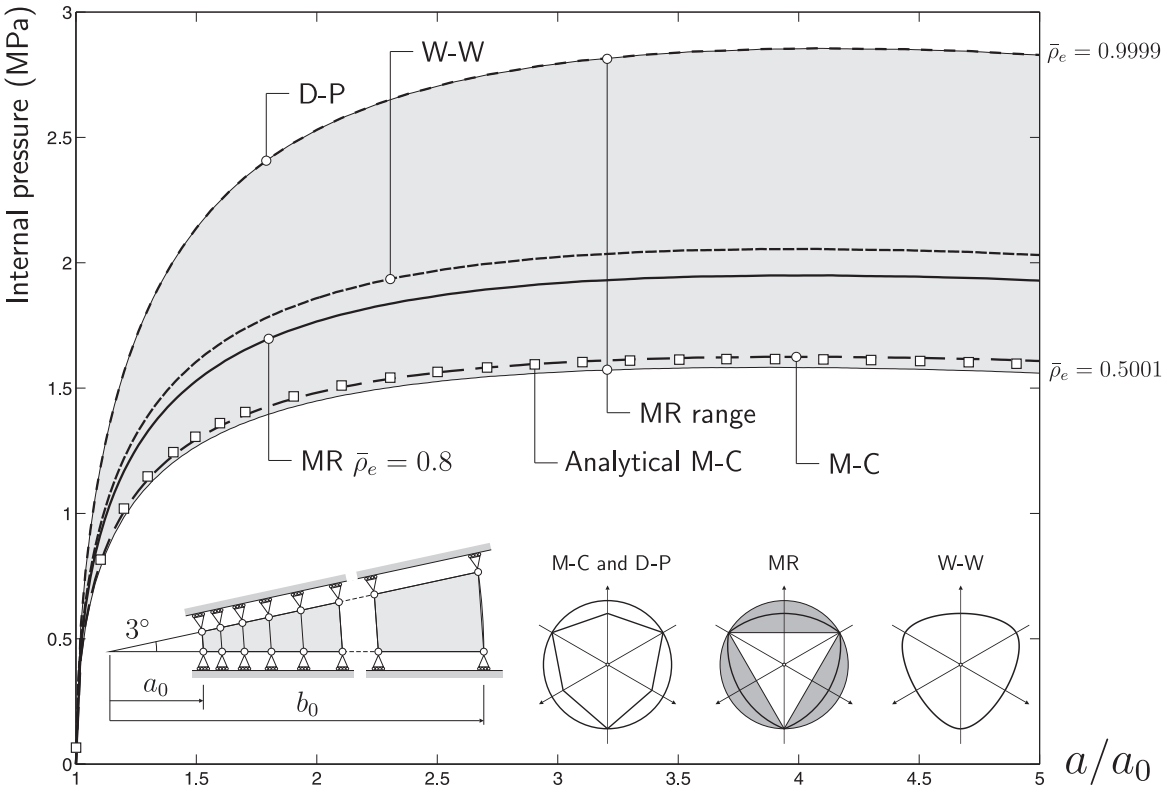

Figure 10: Internal expansion of a thick walled soil cylinder: Comparison between M-C, D-P, W-W and MR constitutive models.

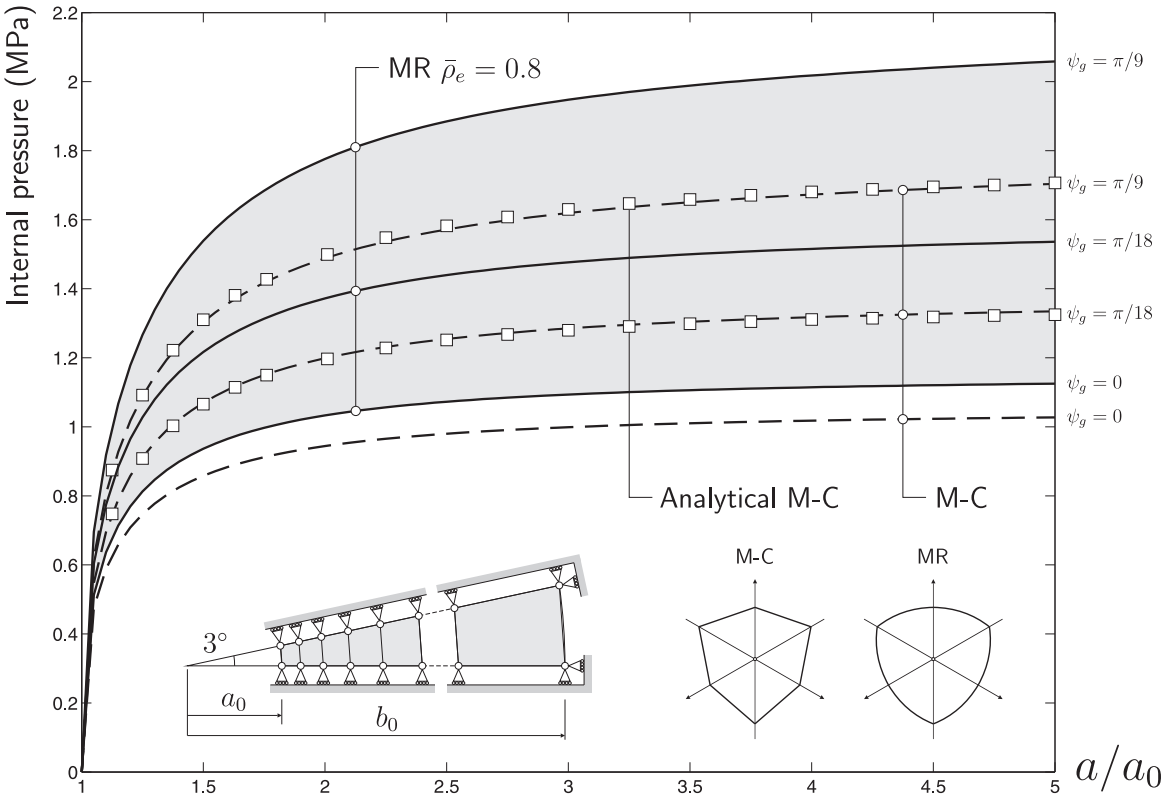

Figure 11: Internal expansion of a cylindrical cavity: Comparison between associated and non-associated flow for Mohr-Coulomb (M-C) and modified Reuleaux (MR) constitutive models .

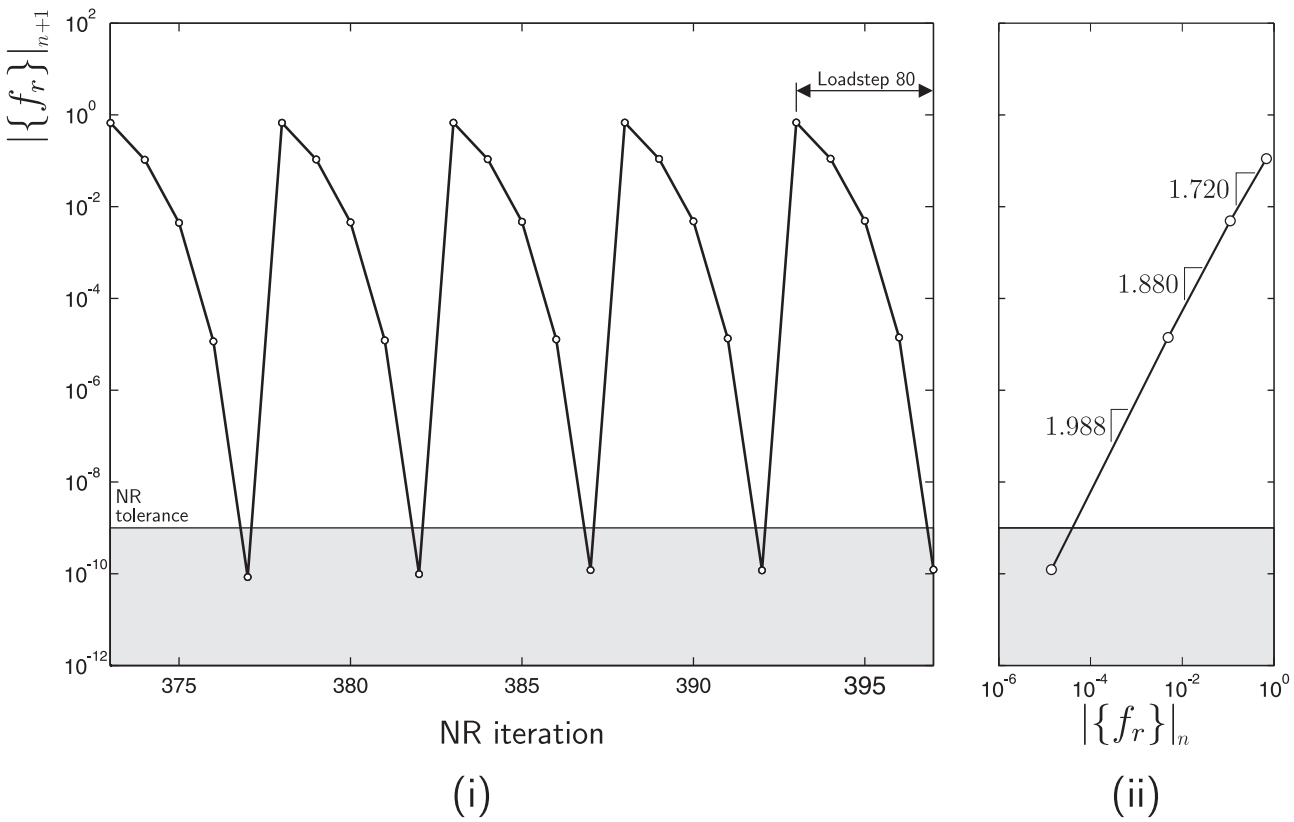

Figure 12: Internal expansion of a cylindrical cavity: convergence results showing (i) the norm of the out-of-balance forces associated with each iteration for the final five loadsteps and (ii) norm of the out-of-balance force against the previous out-of-balance force for the final loadstep for the NAF modified Reuleaux model ($\psi_g = \pi/18$).

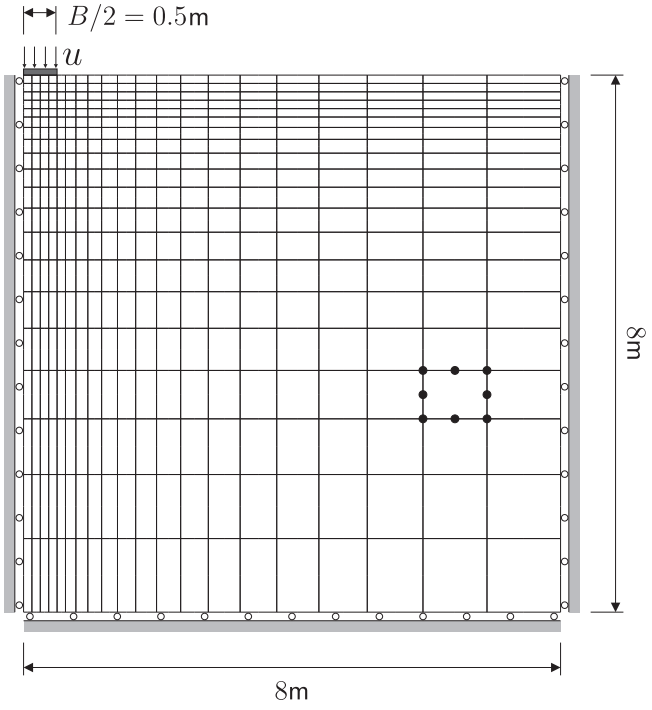

Figure 13: Rigid strip footing plane-strain finite-element discretisation.

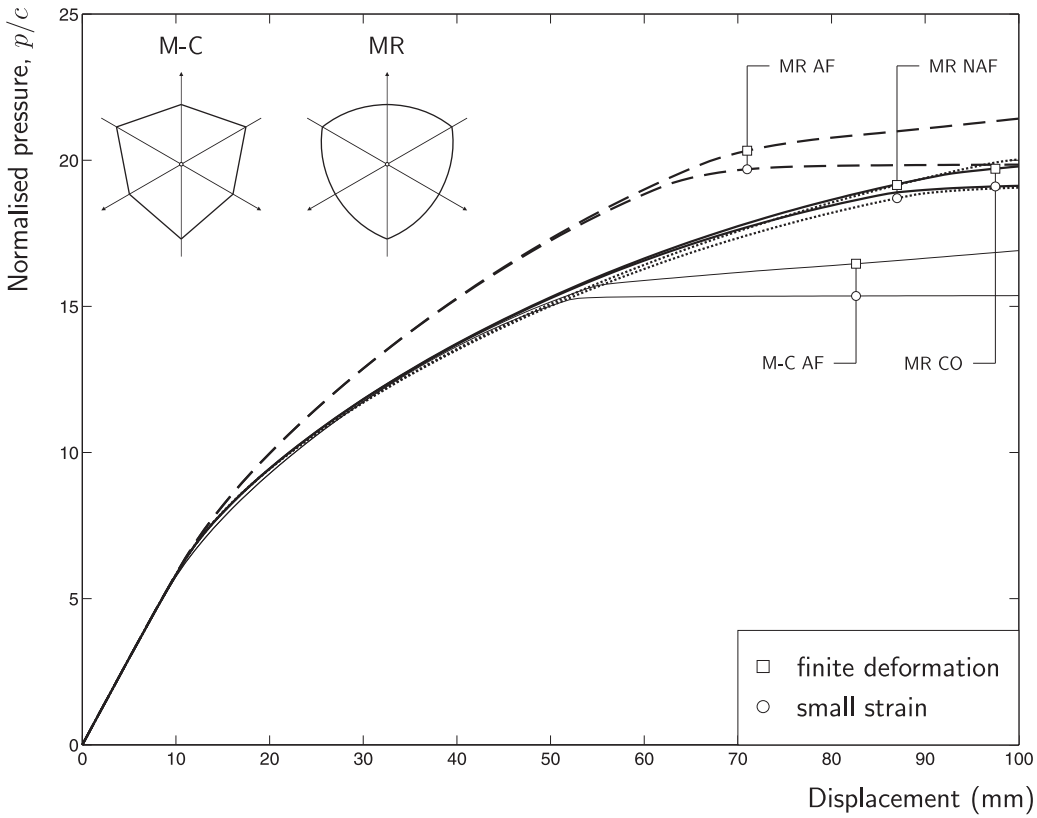

Figure 14: Rigid strip footing normalised pressure-displacement response. MR AF, MR NAF, MR CO and M-C AF denote results from the associated modified Reuleaux, modified Reuleaux non-associated, non-associated modified Reuleaux with a cut-off and associated Mohr-Coulomb models, respectively.

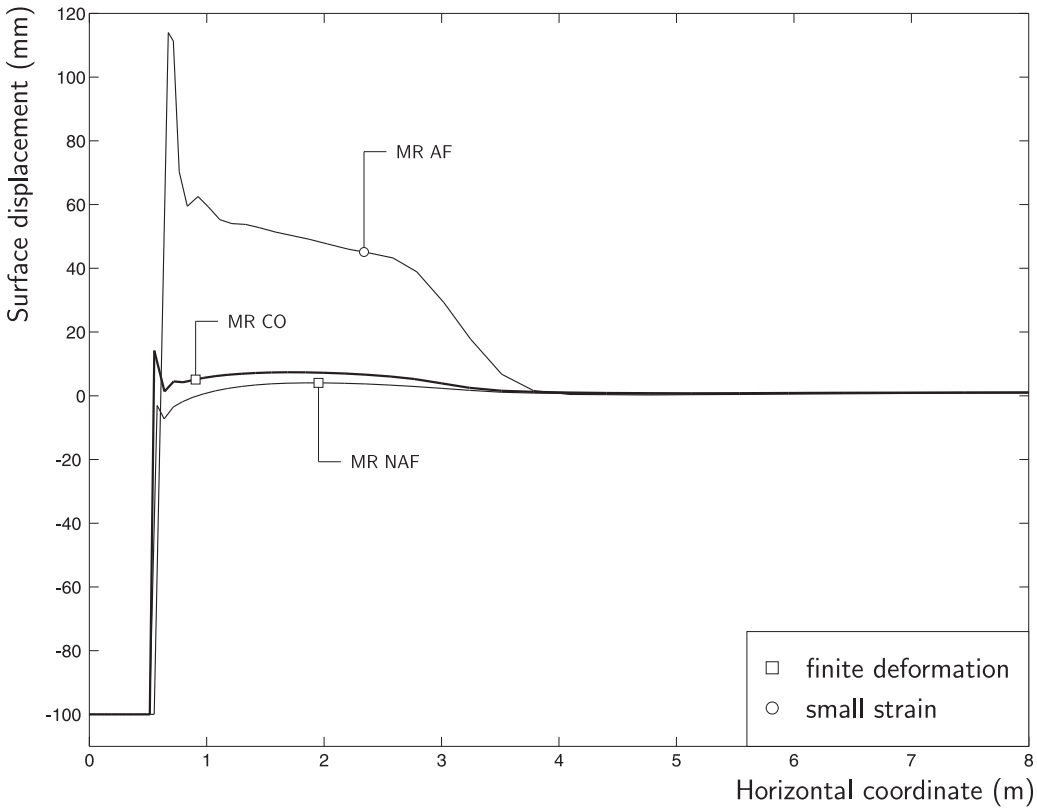

Figure 15: Rigid strip footing surface displacement. MR AF, MR NAF and MR CO denote results from the associated modified Reuleaux, non-associated modified Reuleaux, and non-associated modified Reuleaux with in cut-off respectively.

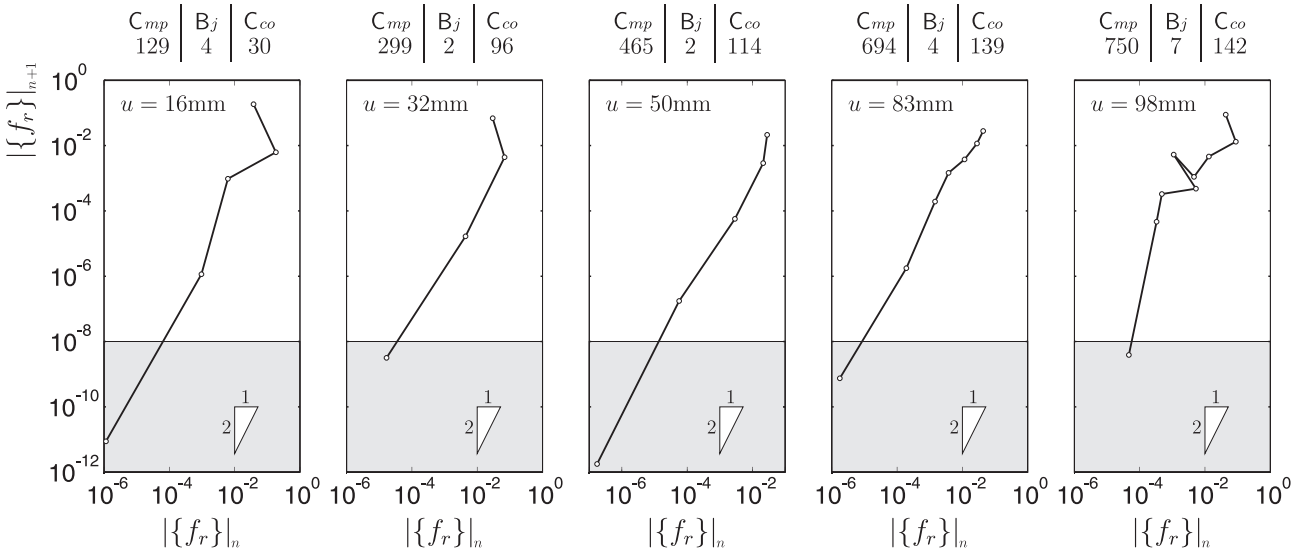

Figure 16: Rigid strip footing convergence for the modified Reuleaux cut-off finite deformation analysis for loadsteps 16, 32, 50, 83 and 98 showing the norm of the out-of-balance force against the previous out-of-balance force. The values above the plots denote the number of elasto-plastic integration points located at different regions of the yield surface.

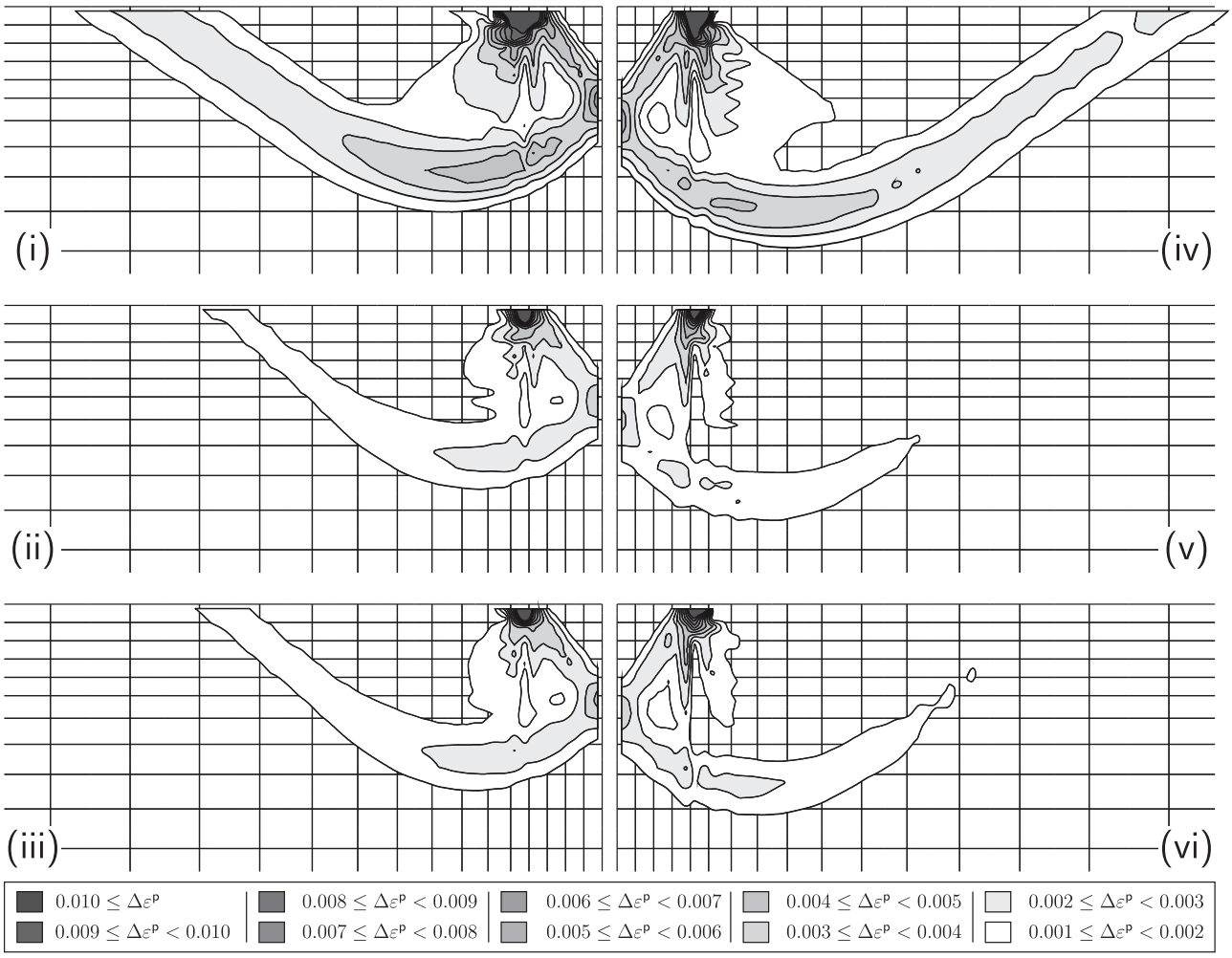

Figure 17: Rigid strip footing: contours of plastic strain increment, $|\{\Delta\varepsilon^{\mathsf{p}}\}|$, for the modified Reuleaux constitutive model during the final loadstep ($\Delta u = -1$mm). (i) small strain AF, (ii) small strain NAF, (iii) small strain NAF with cut-off, (iv) finite deformation AF, (v) finite deformation NAF, (vi) finite deformation NAF with cut-off.

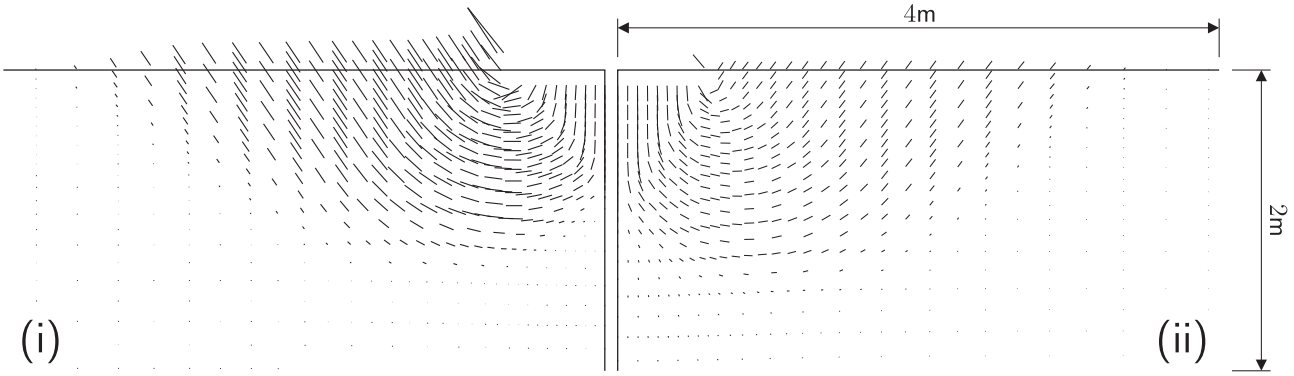

Figure 18: Rigid strip footing: Vectors of nodal displacement for the modified Reuleaux constitutive during the final loadstep $\Delta u = 1$mm (scale factor of 100). (i) small strain AF (ii) finite deformation NAF with cut-off.